Visible light sensing of ions by a cyanoquinoxaline 1,4-dioxide-based probe and its applications

Savita*, Adinarayana Nandikolla*, Adarash Kumar Shukla, Kondapalli Venkata Gowri Chandra Sekhar and Anupam Bhattacharya
Department of Chemistry, Birla Institute of Technology and Science-Pilani (Hyderabad Campus), Hyderabad-500078, India.
E-mail: anupam@hyderabad.bits-pilani.ac.in; Tel: +91-40-66303522.

Supporting Information

Procedure for the synthesis of ACQ/AMQ

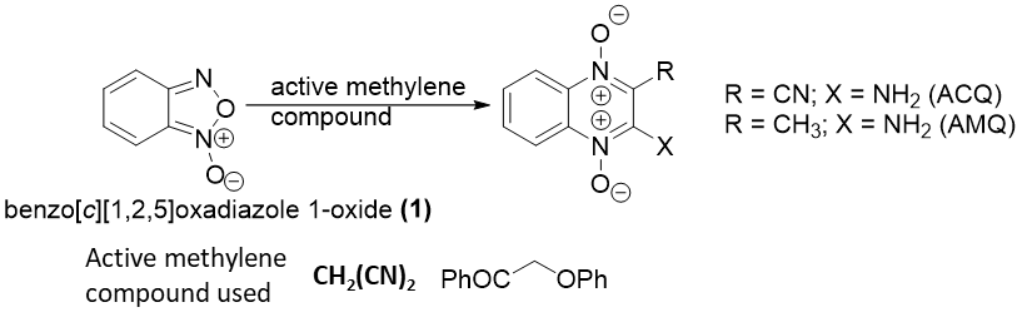

Preparation of ACQ: Malononitrile (1.5 equiv.) was added to a stirred solution of compound **1** (100 mg, 0.73 mmol) [ESI] and triethylamine (3.0 equiv.) in DMF (1 ml). The resulting mixture was then left to stir; on completion of the reaction, as indicated by the TLC, the red precipitate formed was filtered. The resulting solid was washed successively with water and ethyl acetate and dried over the vacuum. Mp: 252-253.2 °C (Lit. Mp: 238-240 °C).[a] Yield: 90 %. ^{1}H NMR (400 MHz, DMSO-d$_6$): δ 8.31 - 8.29 (t, *J* = 7.6 Hz, 2H), 8.07 (s, 2H), 7.94 - 7.91 (m, 1H), 7.68 - 7.64 (m, 1H). ^{13}C NMR (101 MHz, DMSO-d$_6$): δ 146.3, 137.2, 134.6, 132.1, 128.0, 120.1, 118.4, 111.0, 109.1. HRMS-ESI (+) *m/z*: Calcd for $C_9H_7N_4O_2^-$ [M+H$^+$], 203.0574; found, 203.0538.

Preparation of AMQ: 1-Phenoxypropan-2-one (1.1 equiv.) was added to a stirred solution of compound **1** (182 mg, 1.21 mmol) in methanol (5 ml). Ammonia was then purged in the reaction mixture with continuous stirring for 4 hours. On completion of the reaction, as indicated by TLC, the solvent was removed under reduced pressure. The resulting yellow solid was subsequently washed with diethyl ether and dried. Mp: 192-194 °C. Yield: 72.2 %. ^{1}H NMR (400 MHz, DMSO-d$_6$): δ 8.33 (d, *J* = 8 Hz, 1H), 8.235 (d, *J* = 12 Hz, 1H), 7.82(t, *J* = 8Hz, 1H) 7.62 (t, *J* = 8Hz, 1H), 2.55 (s, 3H). ^{13}C NMR (101 MHz, DMSO-d$_6$): 144.9, 134.4, 132.8, 132.1, 131.4, 127.4, 119.6, 117.5, 12.9. HRMS-ESI (+) *m/z*: Calcd for $C_9H_{10}N_3O_2^-$ [M+H$^+$], 192.0779; found, 192.0753.

[a] I. T. Ibrahim and M. A. Wally, *J Radioanal Nucl Chem,* **2010,** 285, 169–175.

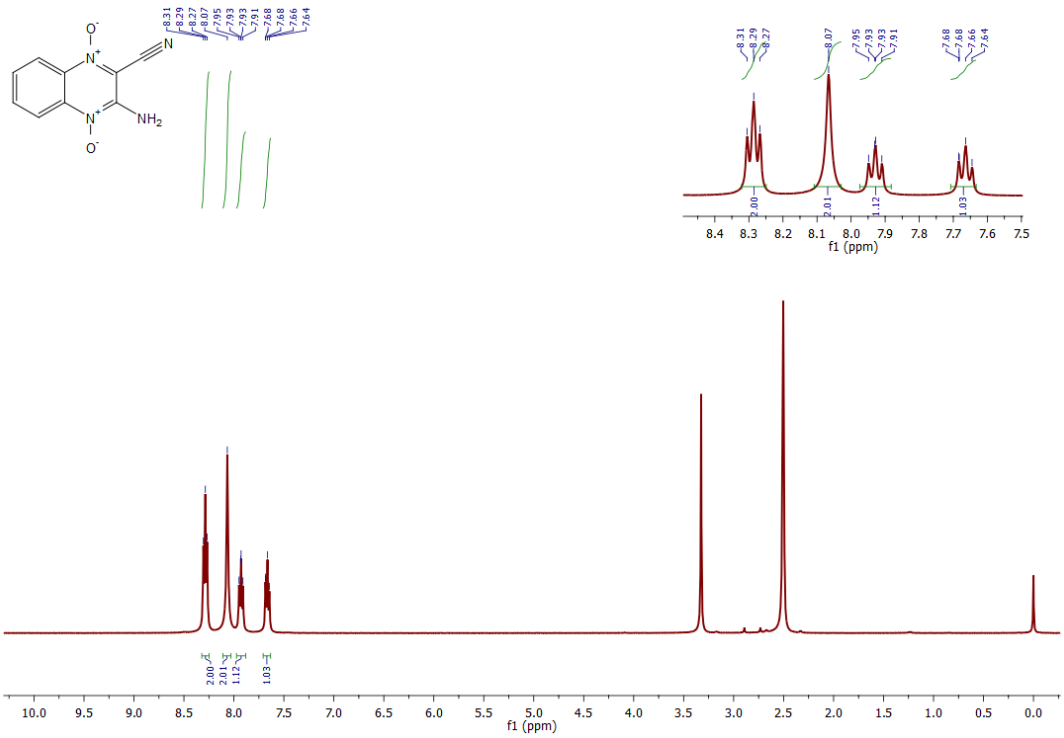

Fig. S1(a) ^{1}H NMR spectrum of **ACQ**

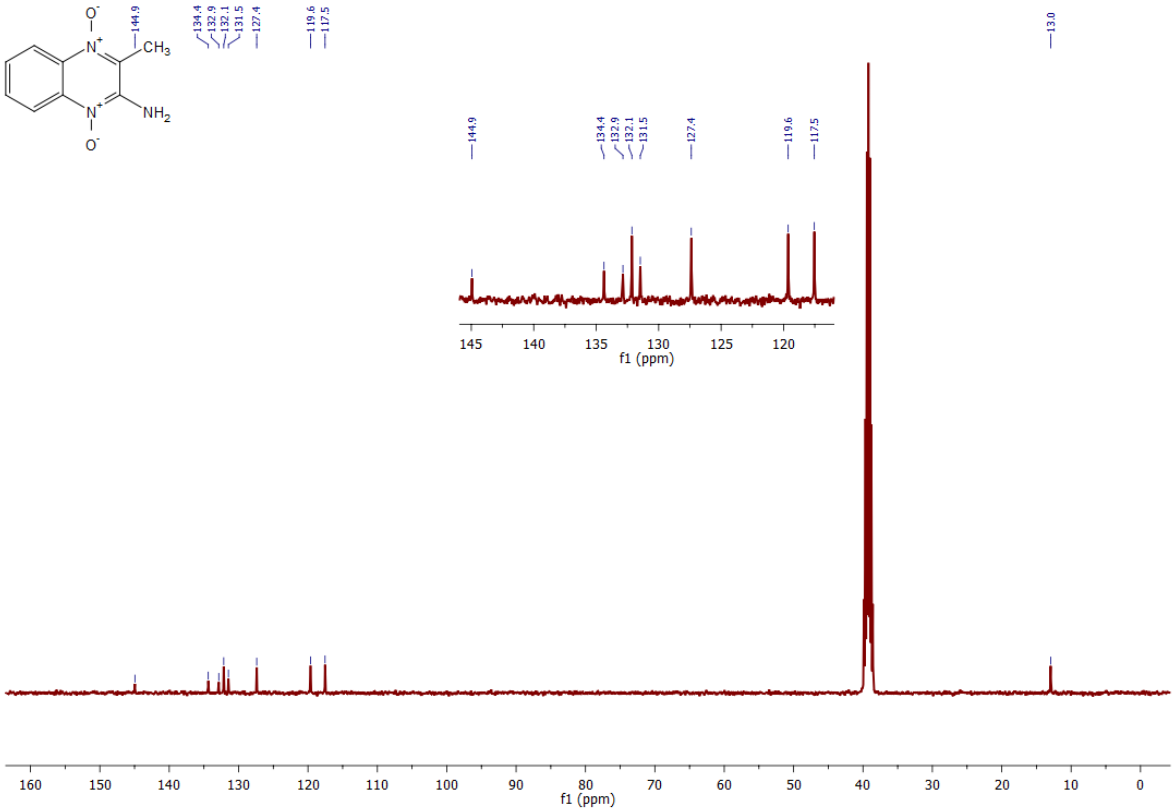

Fig. S1(b) ^{13}C NMR spectrum of **ACQ**

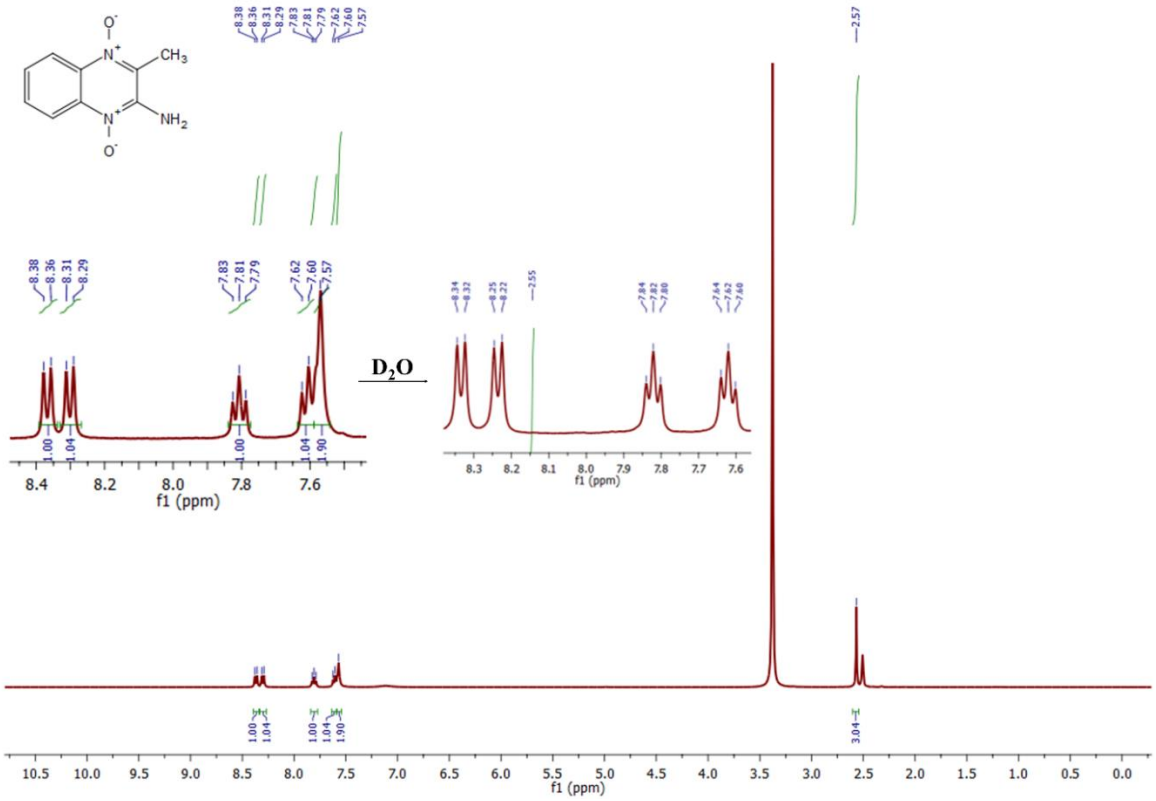

Fig. S2(a) ^{1}H NMR spectrum of **AMQ**

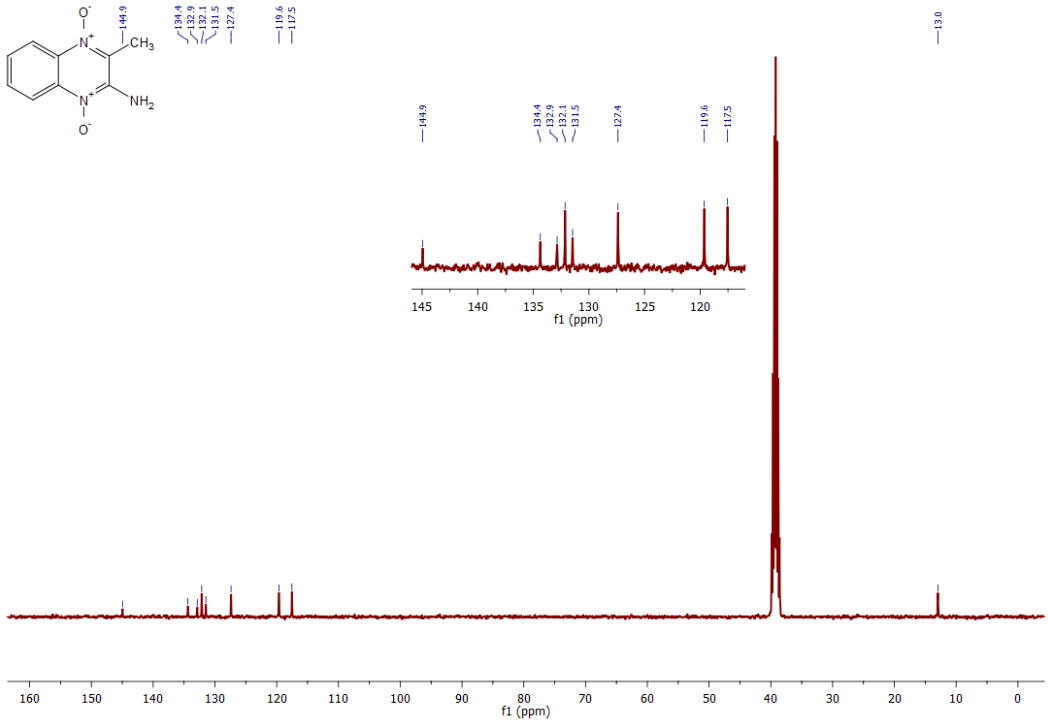

Fig. S2(b) ^{13}C NMR spectrum of **AMQ**

Table. S1 Relative Quantum yield calculation in different solvents

SOLVENT	Dielectric constant (ε)	ACQ λ_{abs} (nm)	ACQ λ_{em} (nm)	Stokes shift (nm)	R_D	ϕ_F
Dioxane	2.3	497	574	77	1.422	0.176
Toluene	2.4	499	570	71	1.4969	0.5206
THF	7.5	507	573	66	1.407	0.8104
DCM	9.1	492	566	74	1.424	0.345
DMF	37	506	586	80	1.430	0.123
ACN	38	498	563	65	1.3441	0.238
DMSO	46.68	505	598	93	1.4793	0.4869
H_2O	80	470	577	107	1.333	0.0082

The following equation was used for calculating quantum yield,

$$\boldsymbol{\Phi}_S = \frac{Abs_R}{Abs_S} \times \frac{Area_S}{Area_R} \times \frac{n_S}{n_R} \times \boldsymbol{\Phi}_R$$

where subscripts S and R refer to the samples and reference respectively. Abs, Area and n are the absorbance at the excitation wavelength, area under the fluorescence spectrum and refractive index of the solvent respectively.

Rhodamine 6G was used as the reference for calculating quantum yield.

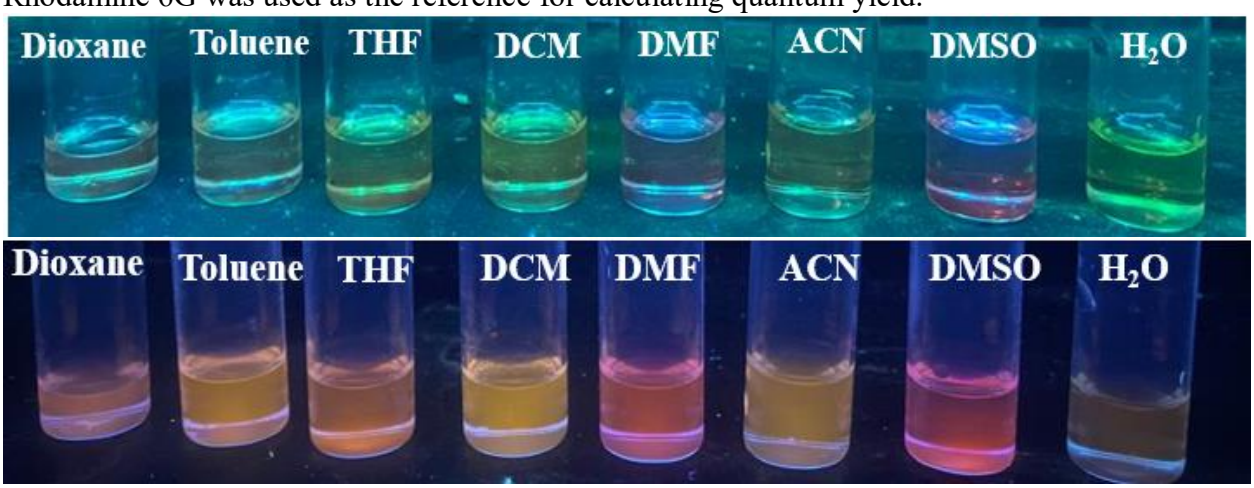

Fig. S3. Photographs under 234 nm and 365 nm for ACQ in different solvents (10 μM)

Calculation of Molar Absorptivity of ACQ

According to Beer-Lambert's Law A = εCl

- A= Absorbance
- C= Molar Concentration (mol L^{-1})
- L=Optical path length (cm)

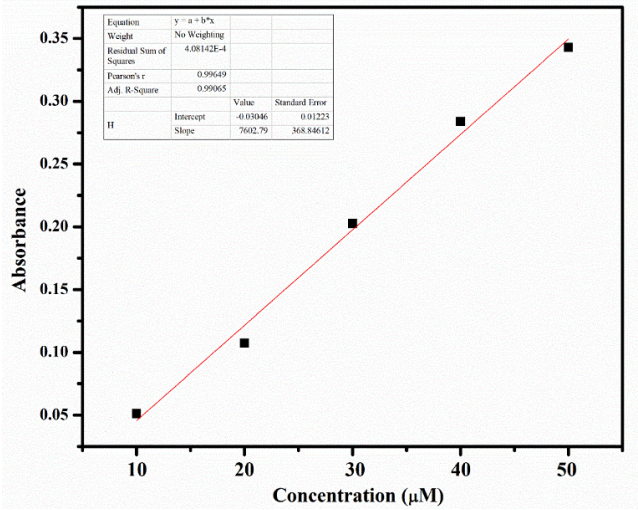

Fig S4. Absorbance versus Concentration plot obtained by varying concentration of ACQ in DMSO from 10 μM – 50 μM. From the value of slope ε =7602.79 L mol^{-1} cm^{-1}

Table S2. Salts used for screening anions against **ACQ** alongside the solvents and concentration, for preparing stock solutions.

S.No.	Anion	Salt	Solvent	Concentration
1.	F^-	Tetrabutylammonium fluoride (TBAF)	DMSO	0.01 M
2.	Cl^-	Tetrabutylammonium chloride (TBACl)	DMSO	0.01 M
3.	Br^-	Tetrabutylammonium bromide (TBAB)	DMSO	0.01 M
4.	I^-	Tetrabutylammonium Iodide (TBAI)	DMSO	0.01 M
5.	OAc^-	Tetrabutylammonium acetate (TBAOAc)	DMSO	0.01 M
6.	$H_2PO_4^-$	Tetrabutylammonium dihydrogen phosphate ($TBAH_2PO_4$)	DMSO	0.01 M
7.	$HSO4^-$	Tetrabutylammonium hydrogensulfate (TBAHSO4)	DMSO	0.01 M
8.	HPO_4^{2-}	Disodium hydrogen phosphate (Na_2HPO_4)	DMSO	0.01 M
9.	SCN^-	Ammonium thiocyanate (NH4SCN)	H_2O	0.01 M
10.	N_3^-	Sodium azide (NaN_3)	H_2O	0.01 M

Table S3. Salts used for screening cations against **ACQ** alongside the solvents and concentration, for preparing stock solutions.

S.No.	Cation	Salt	Solvent	Concentration
1.	Ag^{+}	Silver nitrate ($AgNO_3$)	H_2O	1M
2.	Au^{3+}	Gold (III) chloride trihydrate ($HAuCl_4 \cdot 3H_2O$)	H_2O	0.01 M
3.	Al^{3+}	Aluminum sulfate octa decahydrate ($Al_2(SO_4)_3 \cdot 18H_2O$)	H_2O	0.01 M
4.	Ba^{2+}	Dichlorobarium dihydrate ($BaCl_2 \cdot 2H_2O$)	H_2O	1M
5.	Ca^{2+}	Calcium chloride ($CaCl_2$)	H_2O	1M
6.	Cd^{2+}	Cadmium chloride ($CdCl_2$)	H_2O	1M
7.	Co^{2+}	Cobalt chloride ($CoCl_2$)	H_2O	1M
8.	Cu^{+}	Copper bromide (CuBr)	ACN	1M
9.	Cu^{2+}	Copper sulfate pentahydrate ($CuSO_4 \cdot 5H_2O$)	H_2O	1M
10.	Fe^{2+}	Iron (II) chloride tetrahydrate ($FeCl_2 \cdot 4H_2O$)	H_2O	0.01 M
11.	Fe^{3+}	Ferric chloride ($FeCl_3$)	EtOH	0.01 M
12.	Hg^{2+}	Mercury (II) chloride ($HgCl_2$)	H_2O: EtOH (1:1)	0.01 M
13.	K^{+}	Potassium chloride (KCl)	H_2O	1M
14.	Mg^{2+}	Magnesium dichloride hexahydrate ($MgCl_2.6H_2O$)	H_2O	1M
15.	Mn^{2+}	Manganese (II) Chloride Dihydrate ($MnCl_2.2H_2O$)	H_2O	1M
16.	Na^{+}	Sodium Chloride (NaCl)	H_2O	1M
17.	Ni^{2+}	Nickel (II) chloride hexahydrate ($NiCl_2.6H_2O$)	H_2O	1M
18.	Pb^{2+}	Lead (II) nitrate ($Pb(NO_3)_2$)	H_2O	1M
19.	Pd^{2+}	Palladium (II) acetate ($Pd(ac)_2$)	ACN	0.01 M
20.	Pt^{4+}	Chloroplatinic acid hexahydrate ($H_2PtCl_6 \cdot 6H_2O$)	H_2O	0.01 M
21.	Sn^{2+}	Stannous chloride dihydrate ($SnCl_2.2H_2O$)	H_2O	0.01 M
22.	V^{3+}	Vanadium (III) Chloride (VCl_3)	H_2O	0.01 M
23.	Zn^{2+}	Zinc acetate ($Zn(ac)_2$)	H_2O	1M

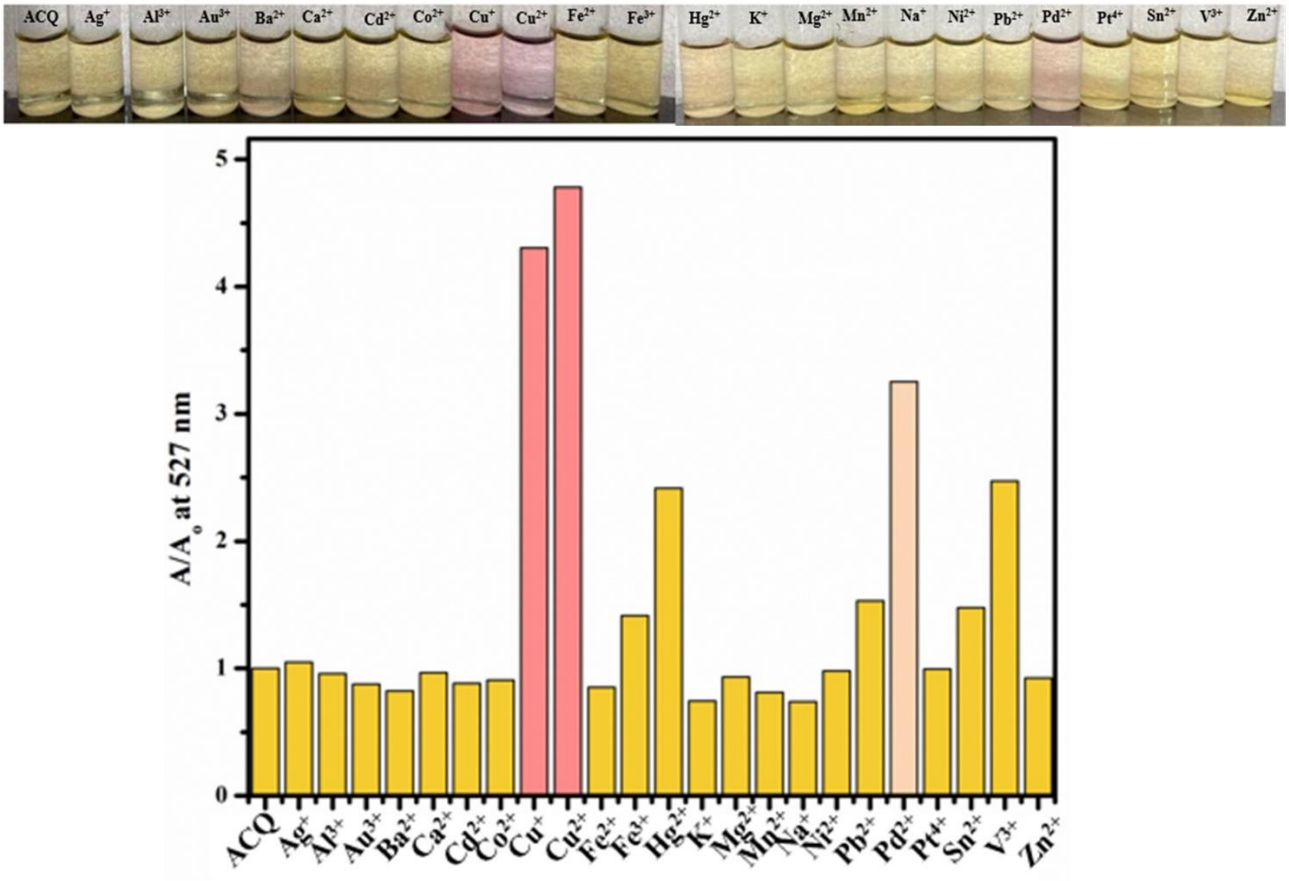

Fig. S5. Bar graph (at 527 nm) of **ACQ** (50μM) in the presence of various cations (1mM) in H_2O.

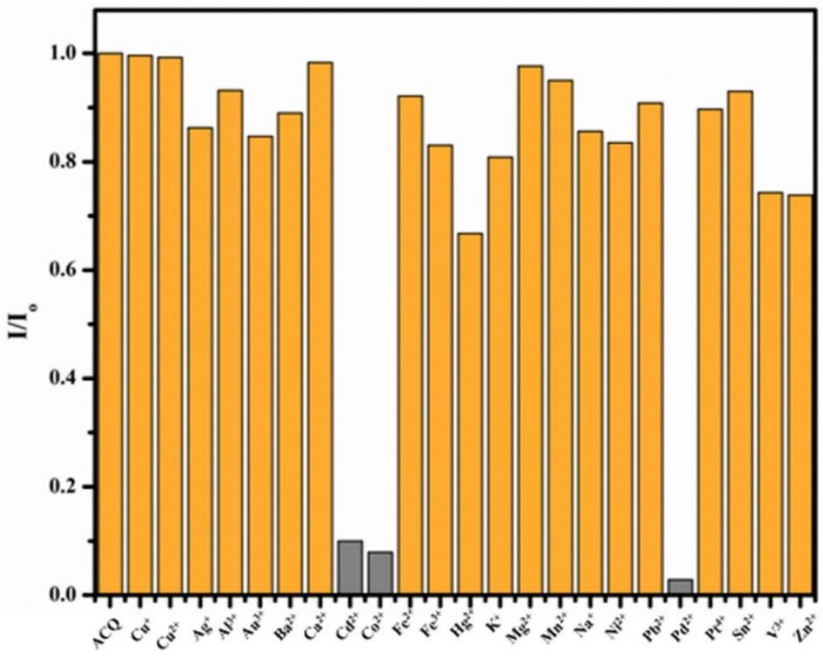

Fig. S6. Bar graph (at 577 nm) of **ACQ** (50μM) in the presence of various anions (1mM) in H_2O.

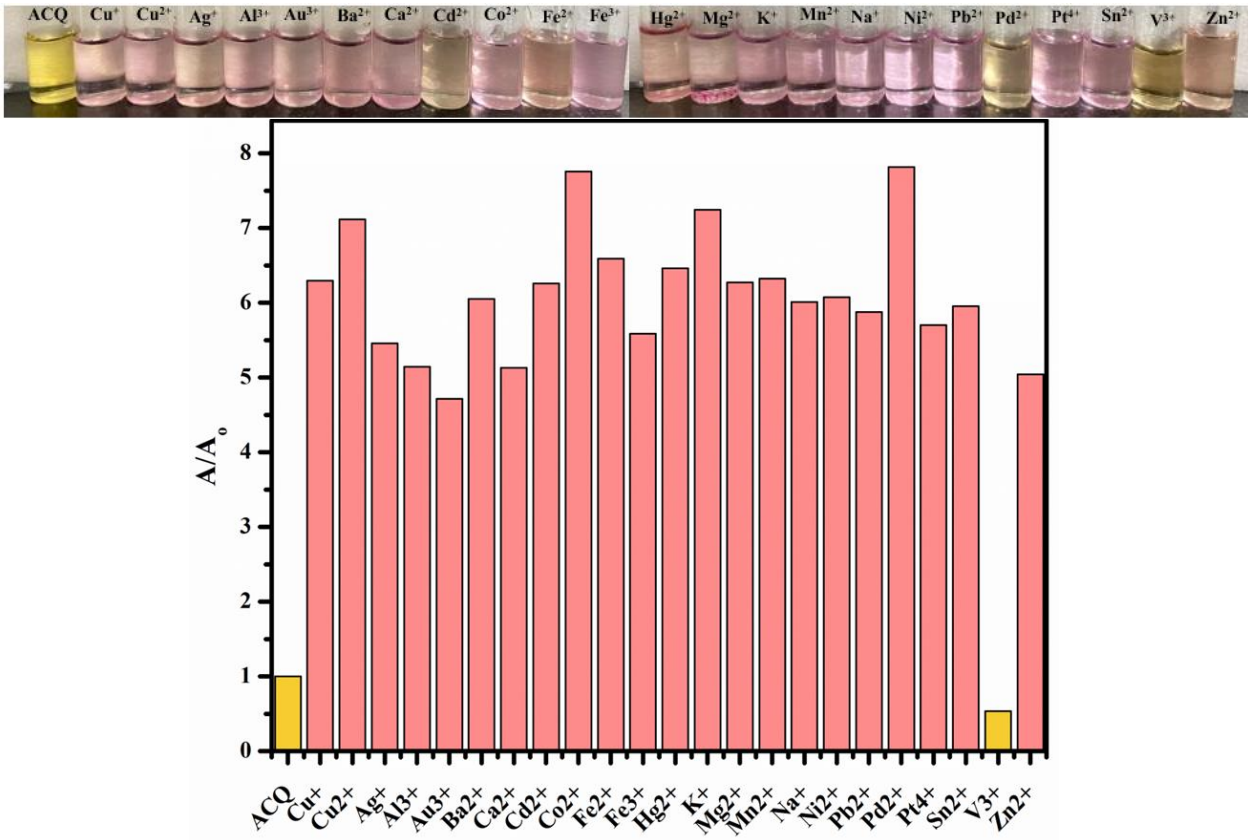

Fig. S7. UV–vis spectra of ACQ (50 μM) in the presence of various competing cations (1 mM) in the presence of Cu^{2+} (50 μM)

- **Interfering Cation: V^{3+}**

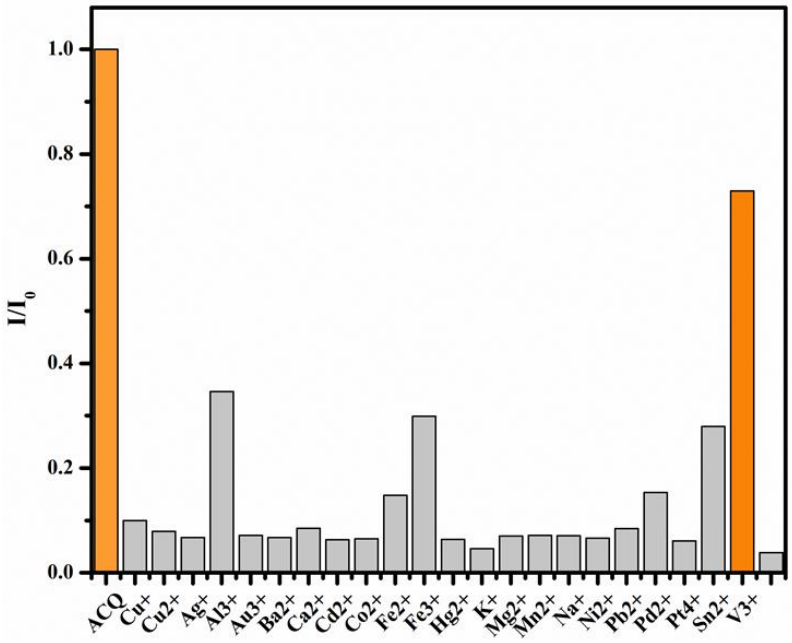

Fig. S8. Intensity of ACQ (50 μM) in the presence of various competing cations (1 mM) in the presence of Cu^{2+} (50 μM)

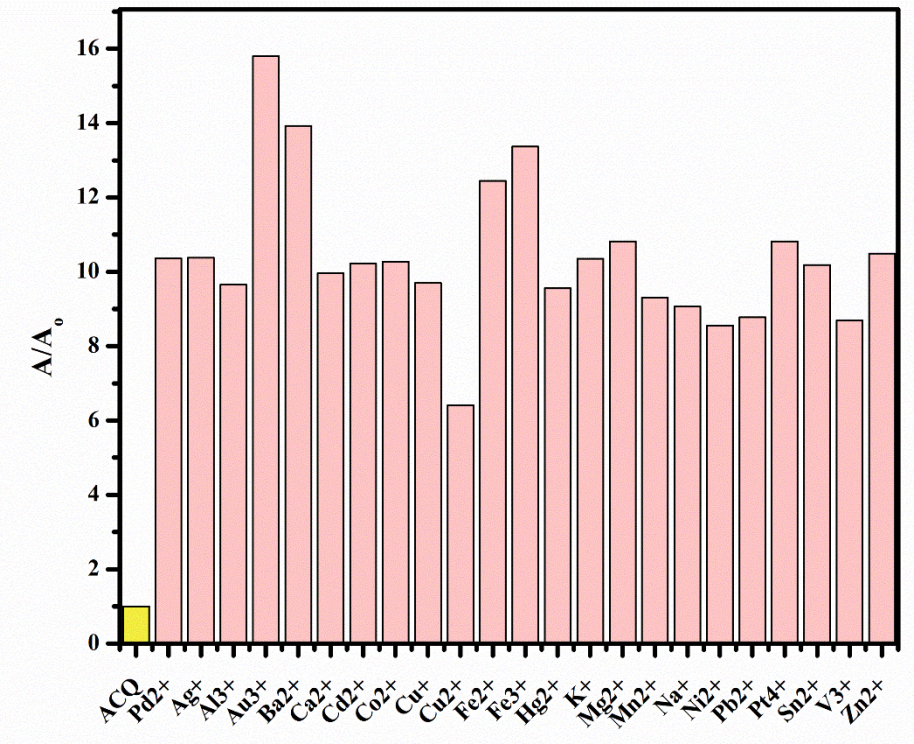

Fig. S9 UV–vis spectra of ACQ (50 μM) in the presence of various competing cations (1 mM) in the presence of Pd^{2+} (200 μM)

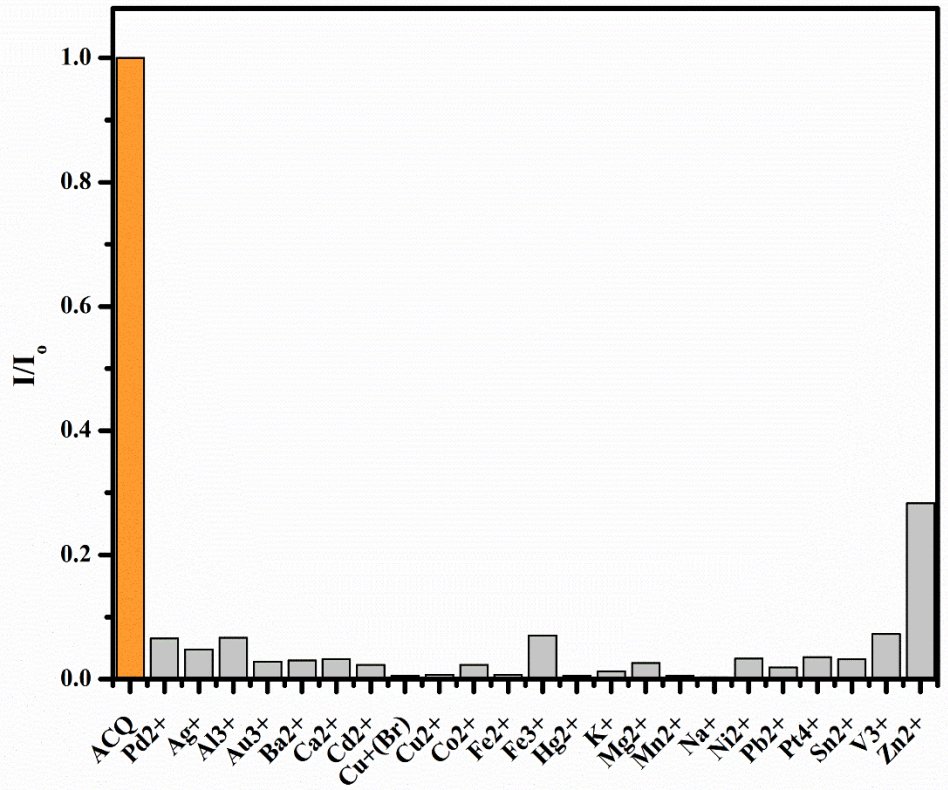

Fig. S10 Intensity of ACQ (50 μM) in the presence of various competing cations (1 mM) in the presence of Pd^{2+} (200 μM)

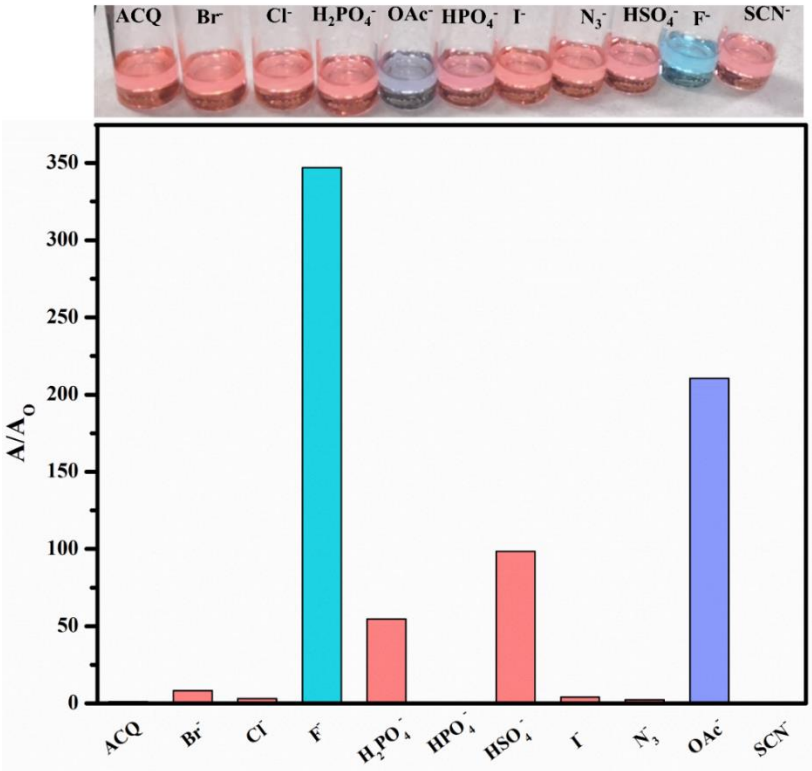

Fig. S11 Bar graph (at 656nm) of **ACQ** (10μM) in the presence of various anions (50μM) in DMSO.

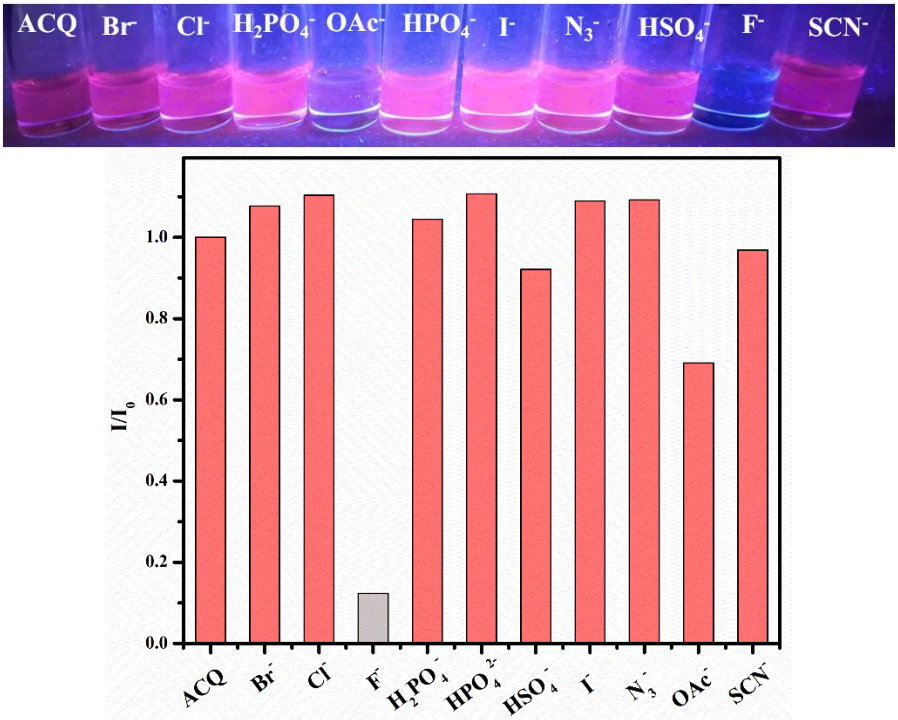

Fig. S12. Bar graph (at 598 nm) of **ACQ** (10μM) in the presence of various anions (50μM) in DMSO. [Side entrance slit: 1.5 nm bandpass; side exit slit: 1.5 nm bandpass]

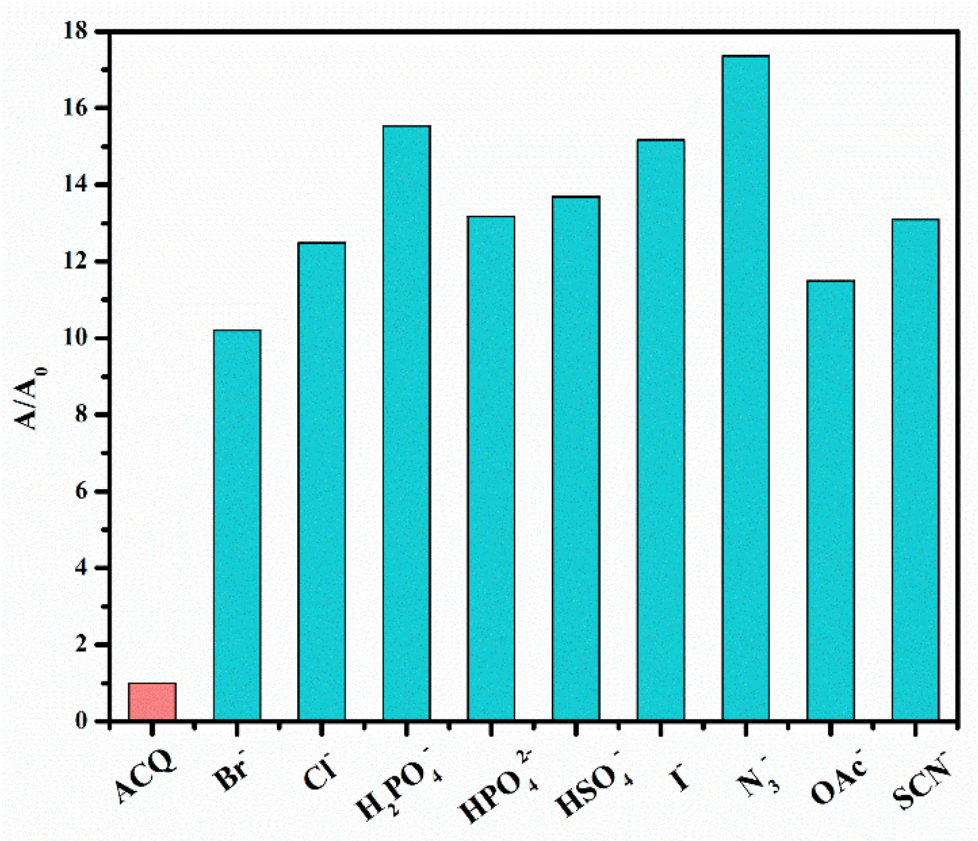

Fig. S13 UV–vis spectra of ACQ (10 μM) in the presence of various competing anions (50μM) in the presence of F^- (50 μM)

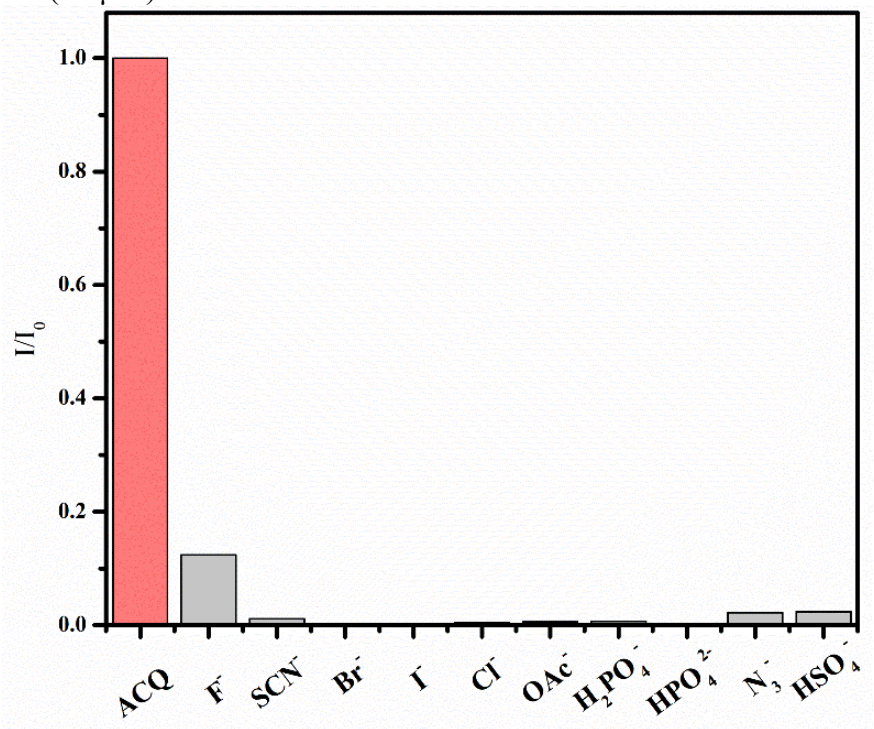

Fig. S14 Intensity of ACQ (10 μM) in the presence of various competing anions (50μM) in the presence of F^- (50 μM).

1. General procedure for determining binding Stoichiometry of ACQ with Cu^{2+}/Pd^{2+}/F^- from Jobs plot:

- Stock solution of same concentration of **ACQ** and analytes (Cu^{2+}, Pd^{2+} and F^-) were prepared in the orders 50μM and 100 μM (in H_2O for Cu^{2+} and Pd^{2+} respectively) and 10 μM (in DMSO for F^-).

- The absorption spectrum in each case by varying the mole fractions (but keeping the volume constant) was recorded.

- Job plots were obtained by plotting absorbance variation value at λ_{max} (527 nm for Cu^{2+} & Pd^{2+} and 656 nm for F^-) versus mole fraction of Cu^{2+}, Pd^{2+} and F^-.

- The maximum value of absorbance was obtained at a mole fraction of X from which the binding ratio of analyte (a) to **ACQ** (l) is determined as

$$\frac{a}{l} = \frac{X}{1 - X}$$

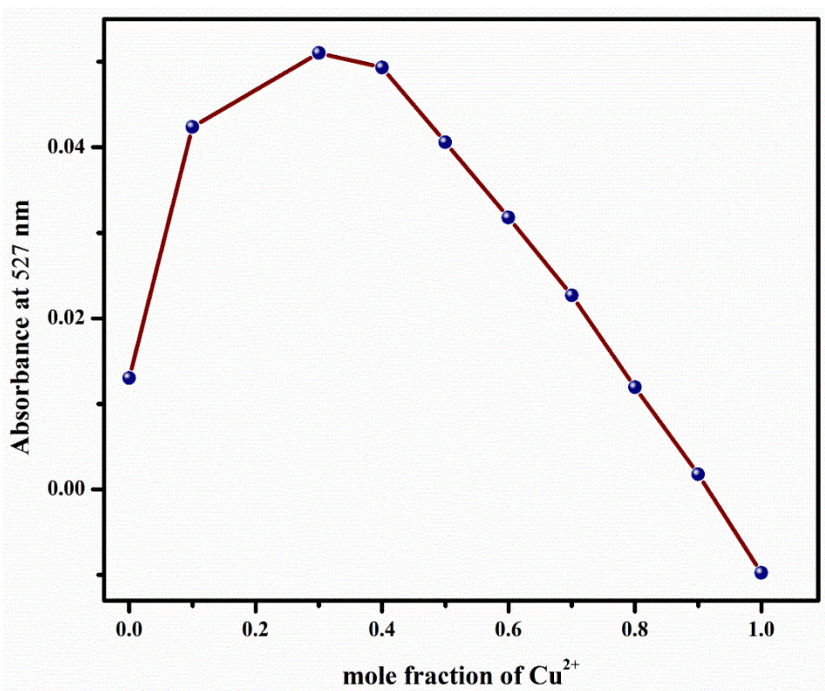

Fig. S15 Absorbance variation value at 527 nm versus Cu^{2+} mole fraction, and the maximum value of absorbance was obtained at a mole fraction of 0.3, indicating a 1:2 (a:l) stoichiometry for the complex between Cu^{2+} and ACQ.

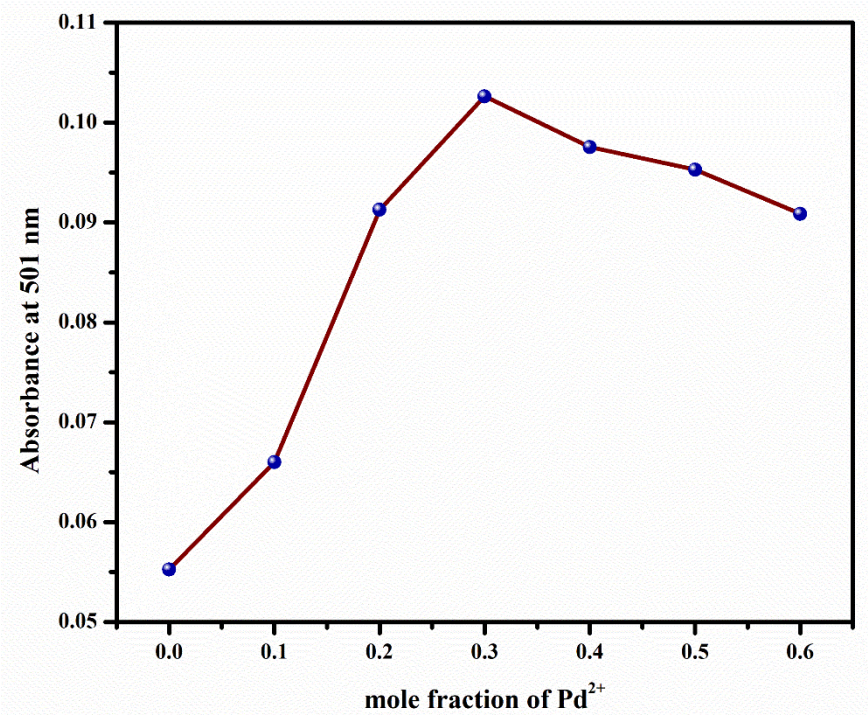

Fig. S16 Absorbance variation value at 527 nm versus Pd^{2+} mole fraction and the maximum value of absorbance was obtained at a mole fraction of 0.3, indicating a 1:2 (a:l) stoichiometry for the complex between Pd^{2+} and ACQ^{-}

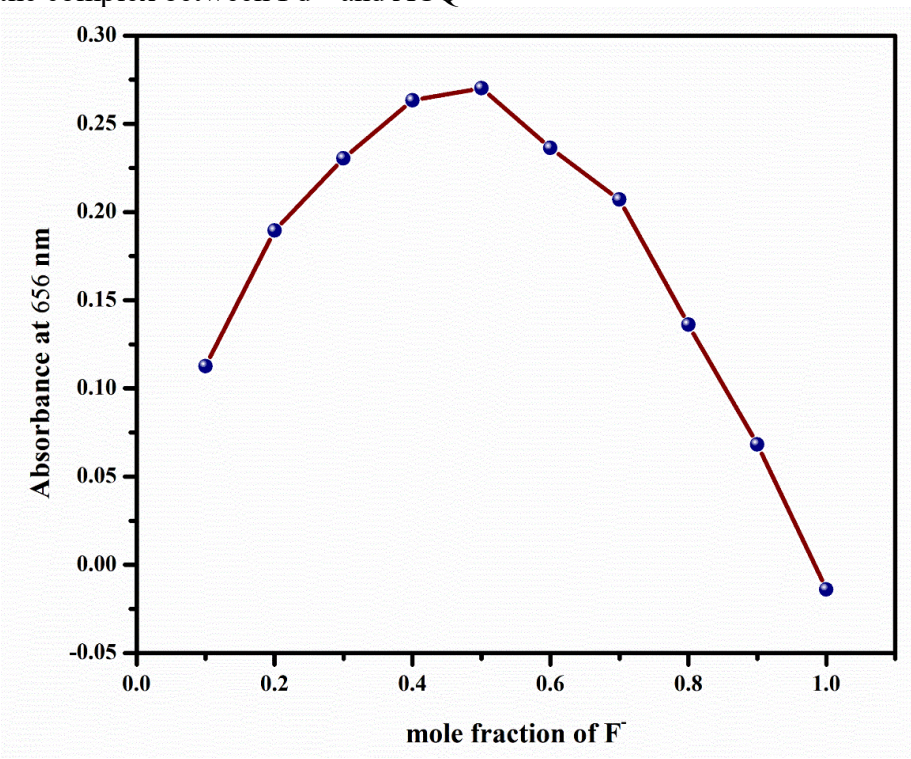

Fig. S17 Absorbance variation value at 656 nm versus F^{-} mole fraction, and the maximum value of absorbance was obtained at a mole fraction of 0.5, indicating a 1:1 (a: l) stoichiometry for the complex between F^{-} and ACQ.

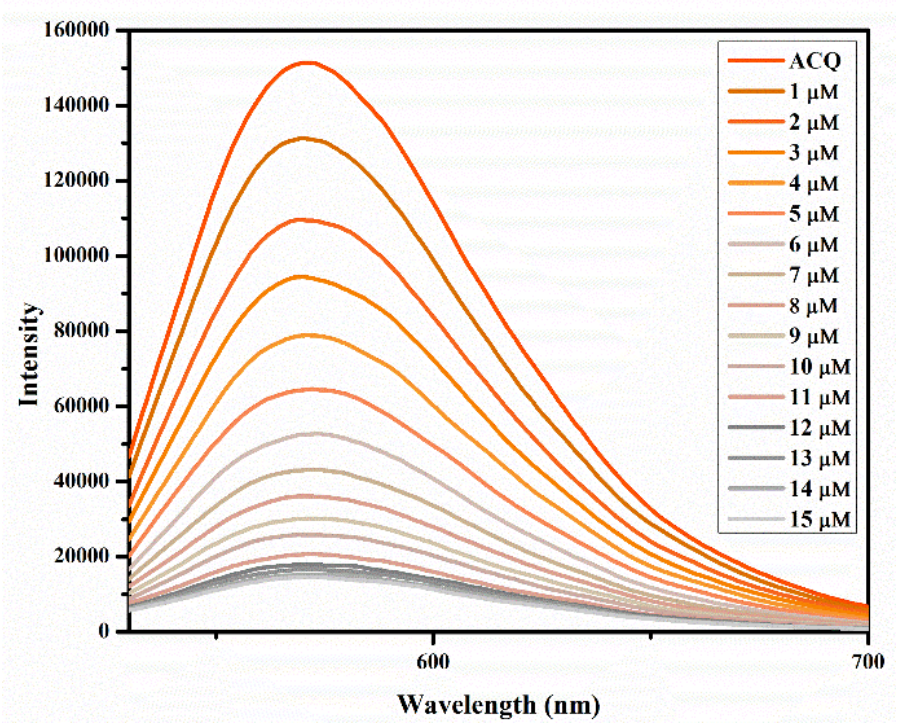

Fig. S18. Fluorescence emission spectra (at 577 nm) of **ACQ** (50 μM) with the addition of various concentrations of Cu^{2+} (0-15 μM) in H_2O respectively

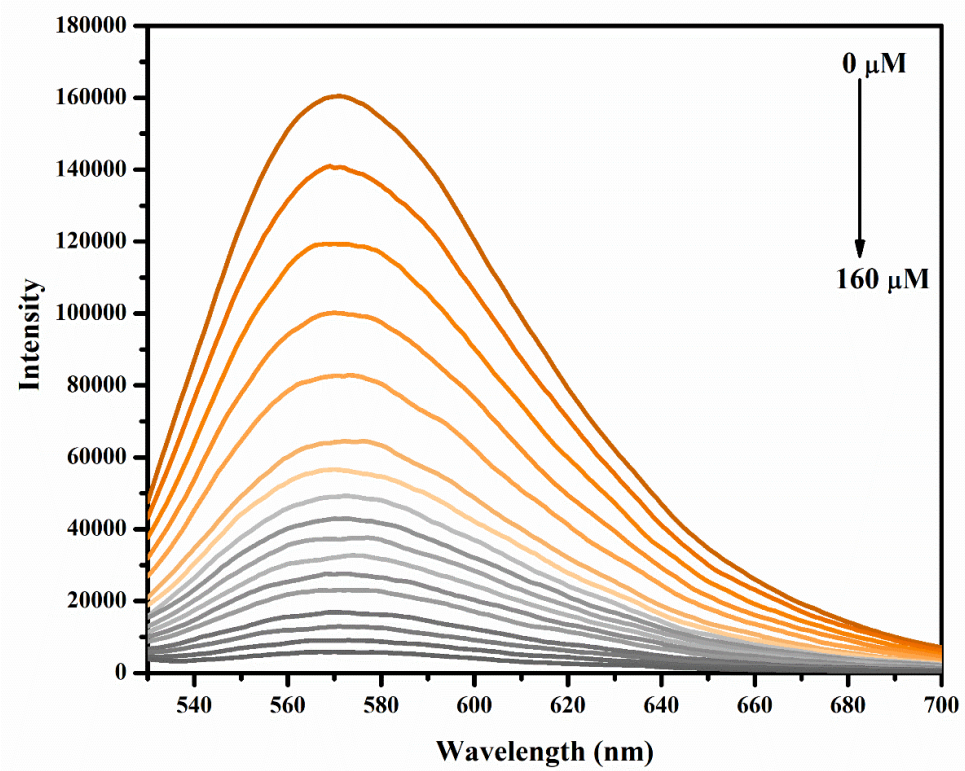

Fig. S19. Fluorescence emission spectra of ACQ (10 μM) with the addition of various concentrations of Pd^{2+}(0-160 μM). [Side entrance slit: 3 nm bandpass; side exit slit: 3 nm bandpass]

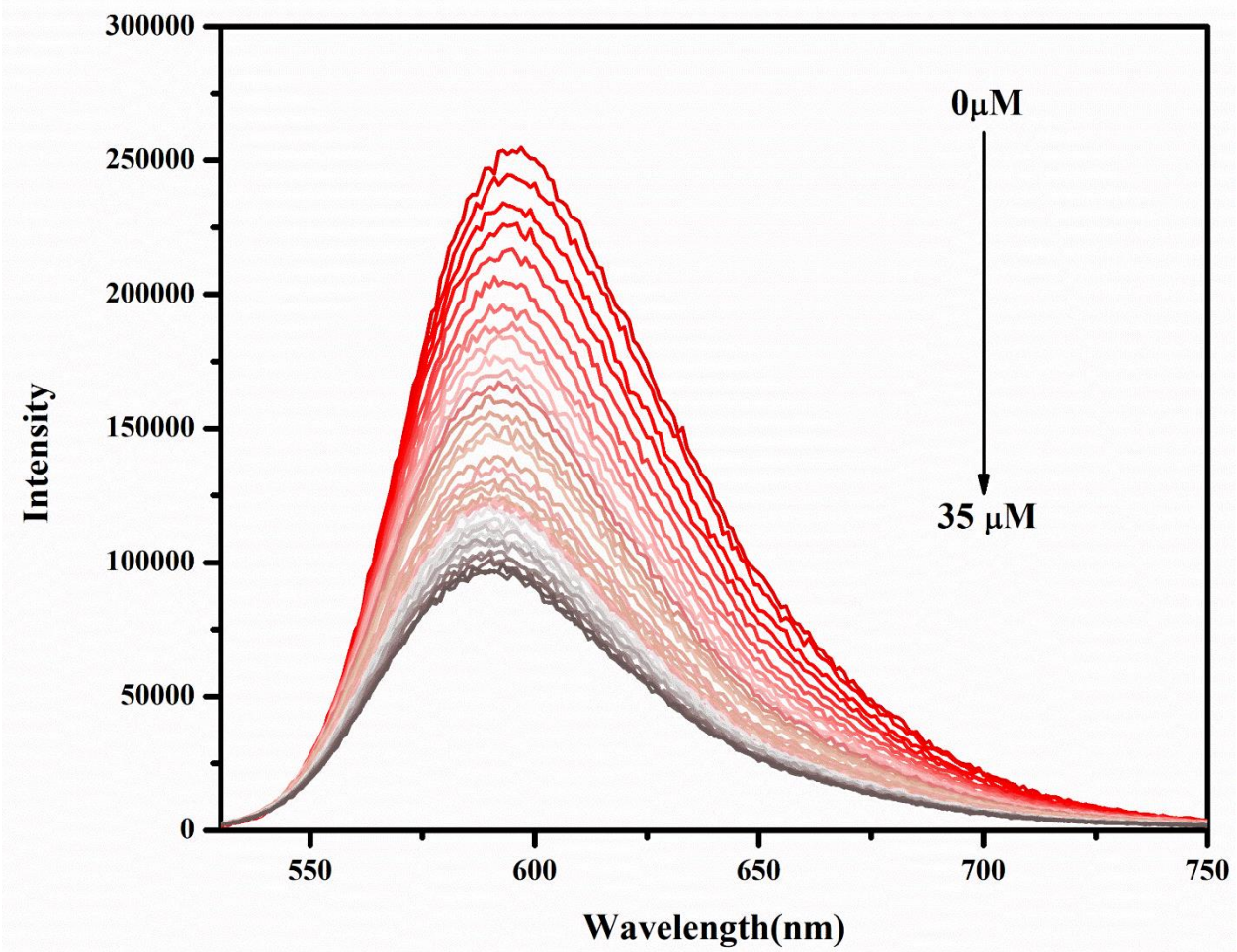

Fig. S20. Fluorescence emission spectra of **ACQ** (10 μM) with the addition of various concentrations of F^-(0-15 μM) and (0-35 μM) respectively

2. Association constant determination:

2a. Using UV Absorbance data:

- Considering a **a: l** ratio stoichiometry for interaction between **ACQ** and $Cu^{2+}/Pd^{2+}/F^-$ as **m**, where **m=(a/l)** binding constant was calculated using

$$\frac{1}{A-A_o} = \frac{1}{(K_a)^m (A_{max}-A_o) [M^{n\pm}]^m} + \frac{1}{(A_{max}-A_o)}$$

- $[M^{n\pm}]$ is the concentration of the $Cu^{2+}/Pd^{2+}/F^-$ ions added during titration studies.
- A_0= absorbance of **ACQ** without $Cu^{2+}/Pd^{2+}/F^-$
- A= absorbance in presence of $Cu^{2+}/Pd^{2+}/F^-$
- A_{max}= absorbance intensity at the maximum concentration of $Cu^{2+}/Pd^{2+}/F^-$
- The value $(K_a)^m$ obtained from the ratio of intercept and slope of Benesi-Hildebrand plot was used to calculate K_a.

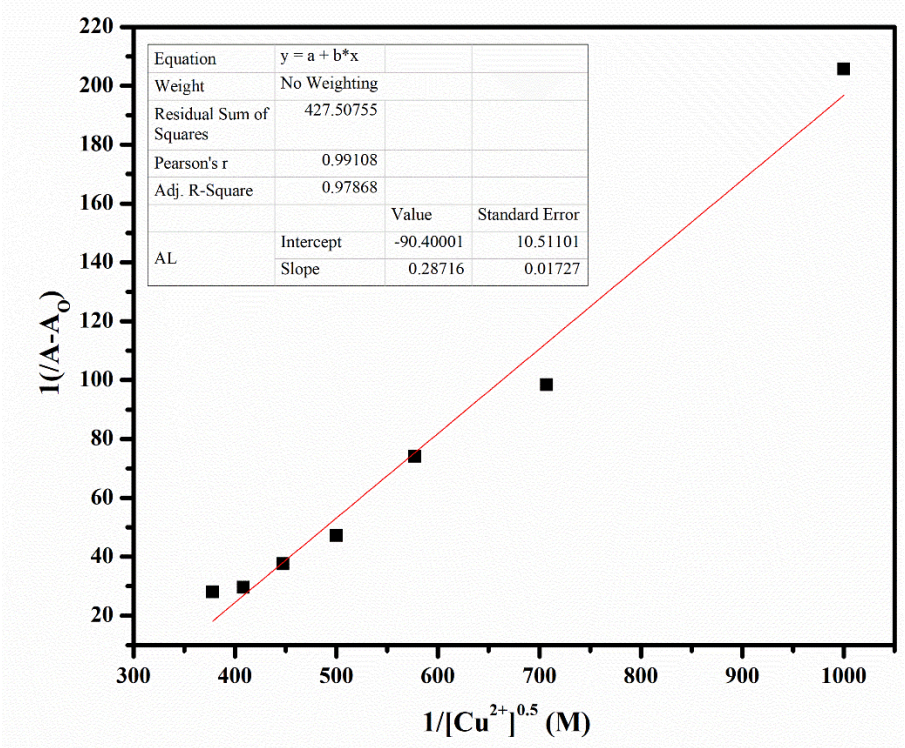

Fig. S21 Benesi–Hildebrand plot from UV-Visible titration data of **ACQ** (50 μM) with Cu^{2+}(0-15 μM). **K_a=9.9 x 10^4 M^{-2}**

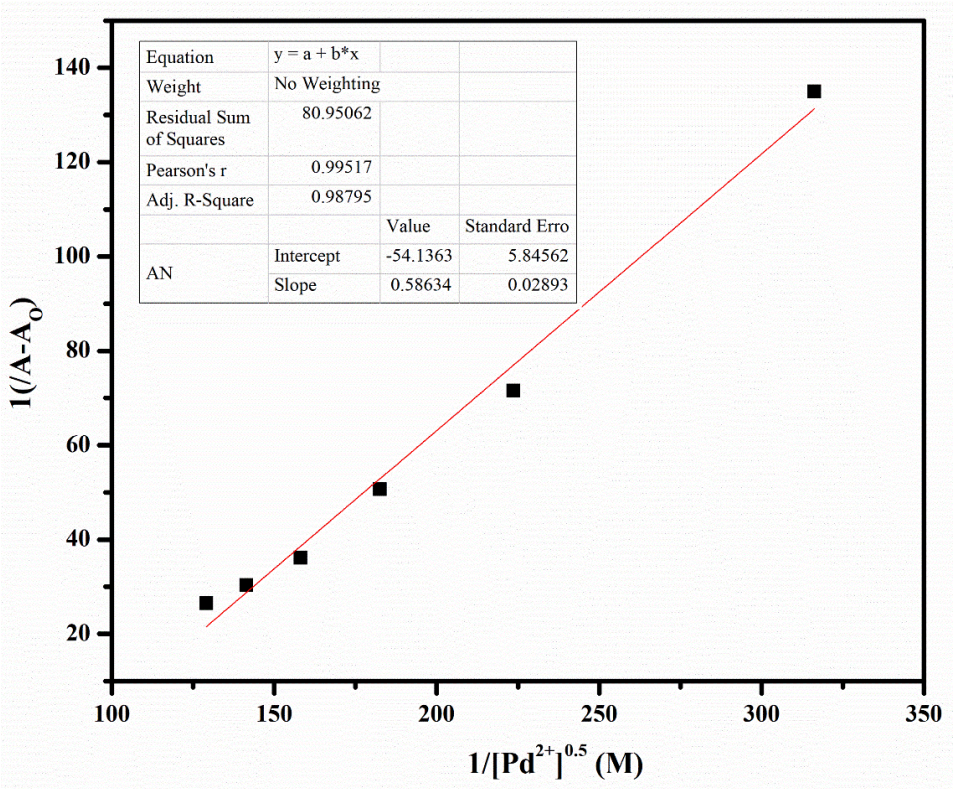

Fig. S22 Benesi–Hildebrand plot from UV-Visible titration data of **ACQ** (50 μM) with Pd^{2+}(0-150 μM). **K_a=8.7 x 10^3 M^{-2}**

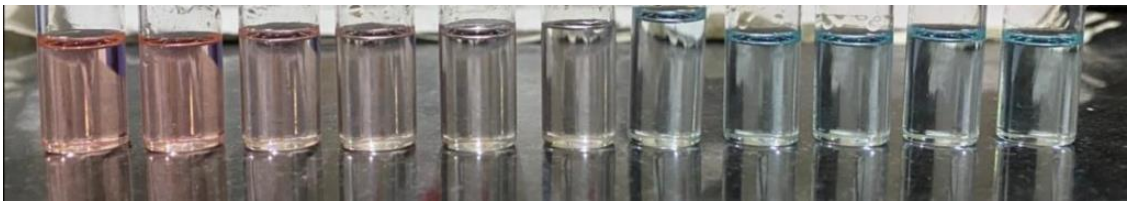

Fig. S23. Visible color changes of ACQ (50 μM) on continuous addition of F^- ions (0-15 μM)

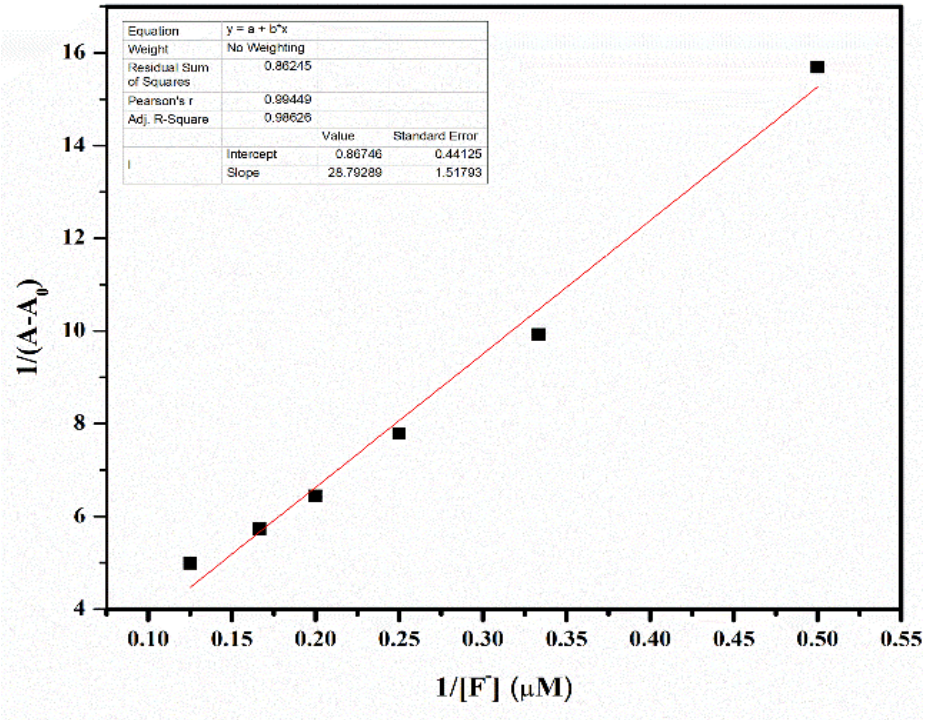

Fig. S24 Benesi–Hildebrand plot from UV-Visible titration data of **ACQ** (10 μM) with F^- (0-15 μM). $\mathbf{K_a = 5.8x\ 10^4\ M^{-1}}$

2b. Using emission intensity data:

- Considering a **a:l** ratio stoichiometry for interaction between **ACQ** and $Cu^{2+}/Pd^{2+}/F^-$ as **m**, where **m=(a/l)** binding constant was calculated using

$$\frac{1}{F-F_o} = \frac{1}{(K_a)^m\,(F_{max}-F_o)\,[M^{n\pm}]^m} + \frac{1}{(F_{max}-F_o)}$$

- $[M^{n\pm}]$ is the concentration of the $Cu^{2+}/Pd^{2+}/F^-$ ions added during titration studies.
- F_0= fluorescence intensity of **ACQ** without $Cu^{2+}/Pd^{2+}/F^-$
- F= fluorescence intensity in presence of $Cu^{2+}/Pd^{2+}/F^-$
- F_{max}= fluorescence intensity at the maximum concentration of $Cu^{2+}/Pd^{2+}/F^-$
- The value $(K_a)^m$ obtained from the ratio of intercept to slope of the linear plot between $1/(F-F_0)$ vs $1/[M^{n\pm}]^m$ was used to calculate K_a.

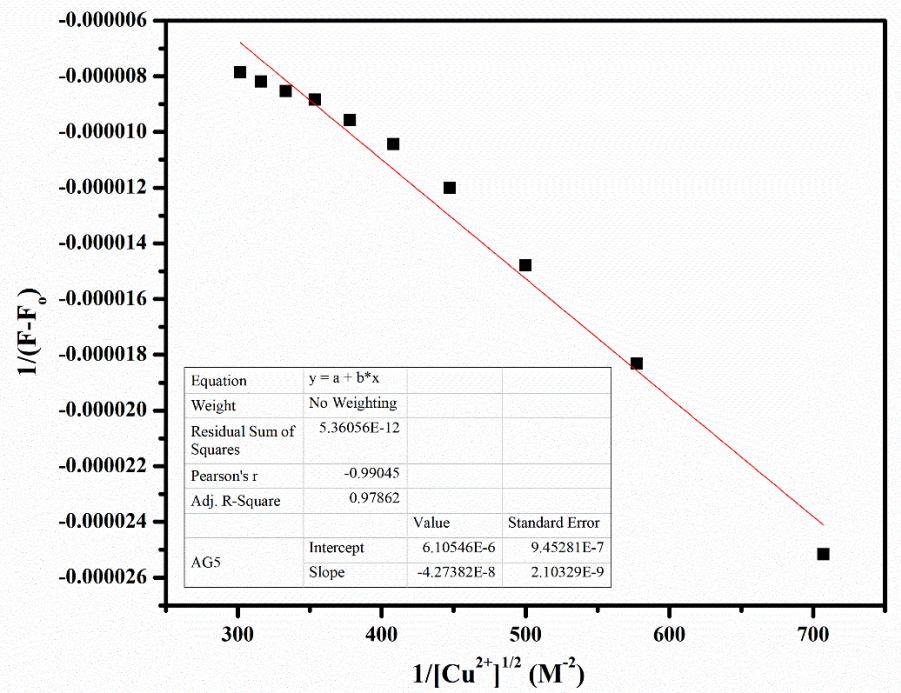

Fig. S25 Benesi–Hildebrand plot from fluorescence titration data of **ACQ** (50 μM) with Cu^{2+}(0-15 μM). **K_a=3.18 x 10^4 M^{-2}**

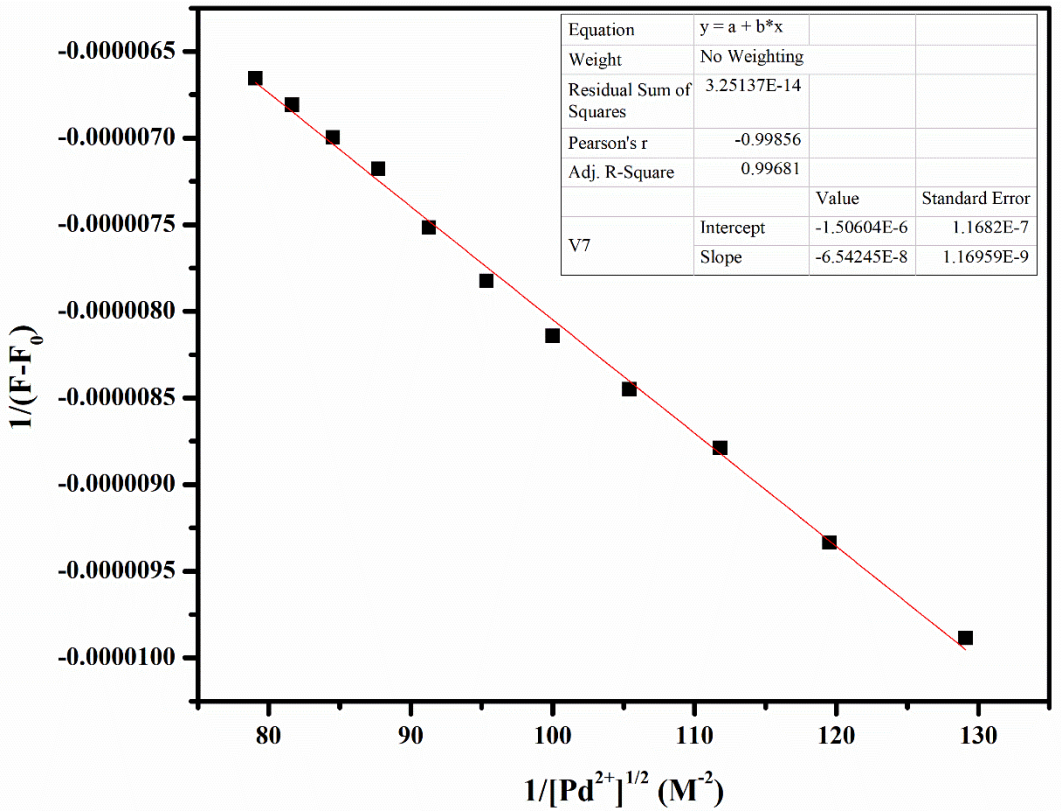

Fig. S26 Benesi–Hildebrand plot from fluorescence titration data of **ACQ** (50 μM) with Pd^{2+}(0-160 μM). **K_a=0.5 x 10^3 M^{-2}**

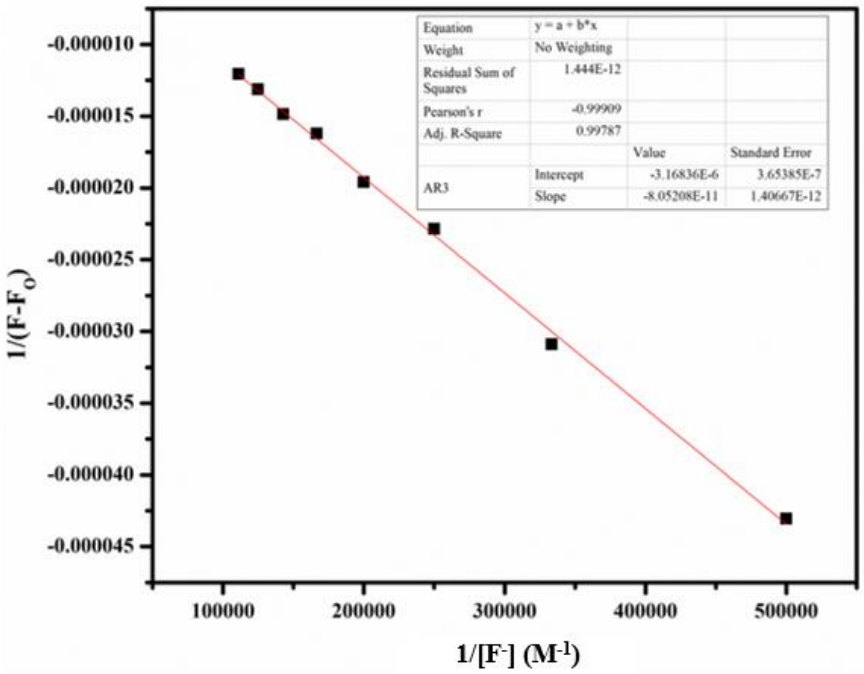

Fig. S27 Benesi–Hildebrand plot from fluorescence titration data of **ACQ** (10 μM) with F^- (0-35 μM). **K_a=3.8 x 10^4 M^{-1}**

3. Determination of detection limit

LOD was calculated using this formula **3σ/K** where;

- K is Slope value taken from Absorbance/Intensity vs Concentration of Cu^{2+}/ Pd^{2+}/ F^- plot
- σ is the standard deviation of the blank solution

3a. Using UV Absorbance data:

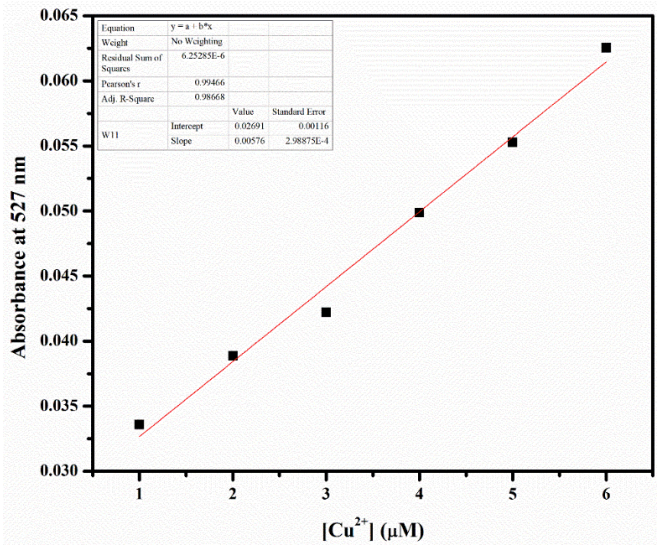

Fig. S28 Plot of Absorbance versus concentration of Cu^{2+} at 527 nm and the calculated limit of Detection of ACQ for Cu^{2+} is 0.75 μM

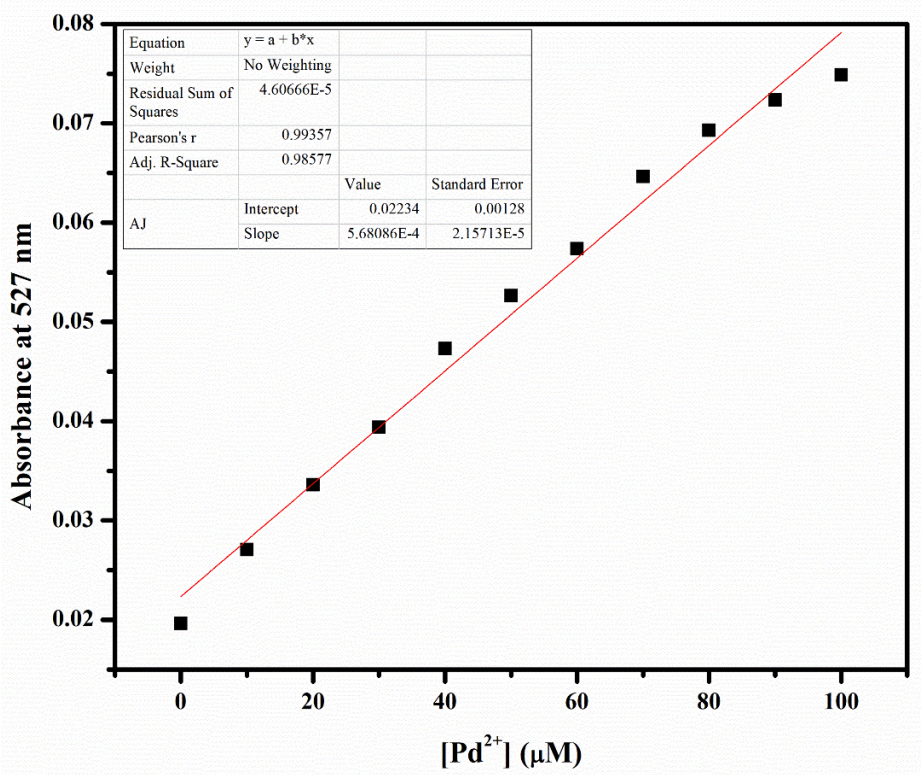

Fig.S29 Plot of Absorbance versus concentration of Pd^{2+}at 527 nm and the calculated limit of Detection of ACQ for Pd^{2+} is 7.6 μM

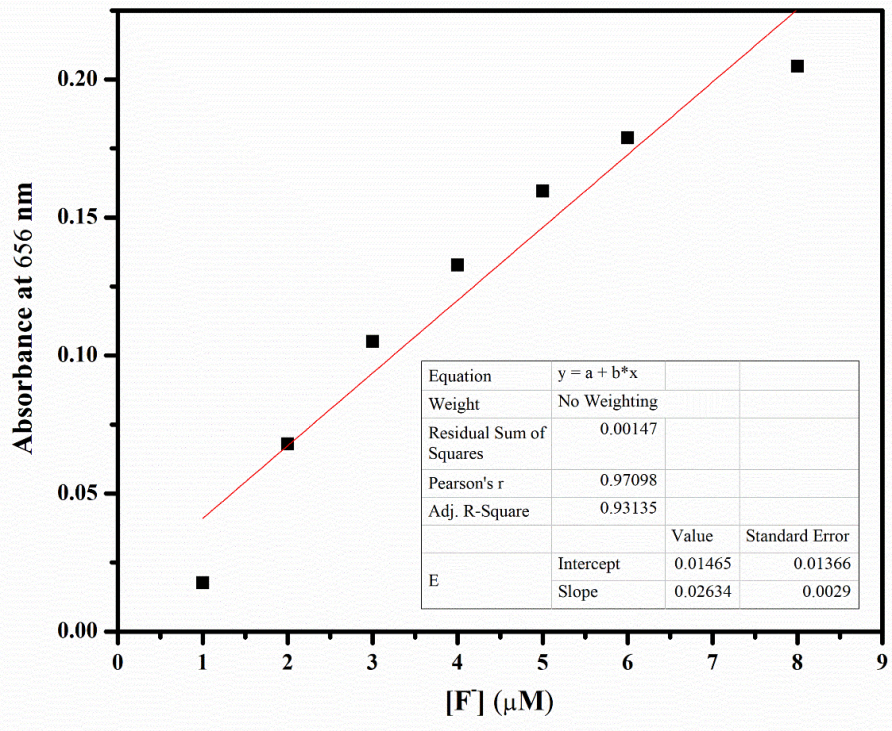

Fig. S30 Plot of Absorbance versus concentration of F^- at 656 nm and the calculated limit of Detection of ACQ for F^- is 0.53 μM

3b. Using emission intensity data:

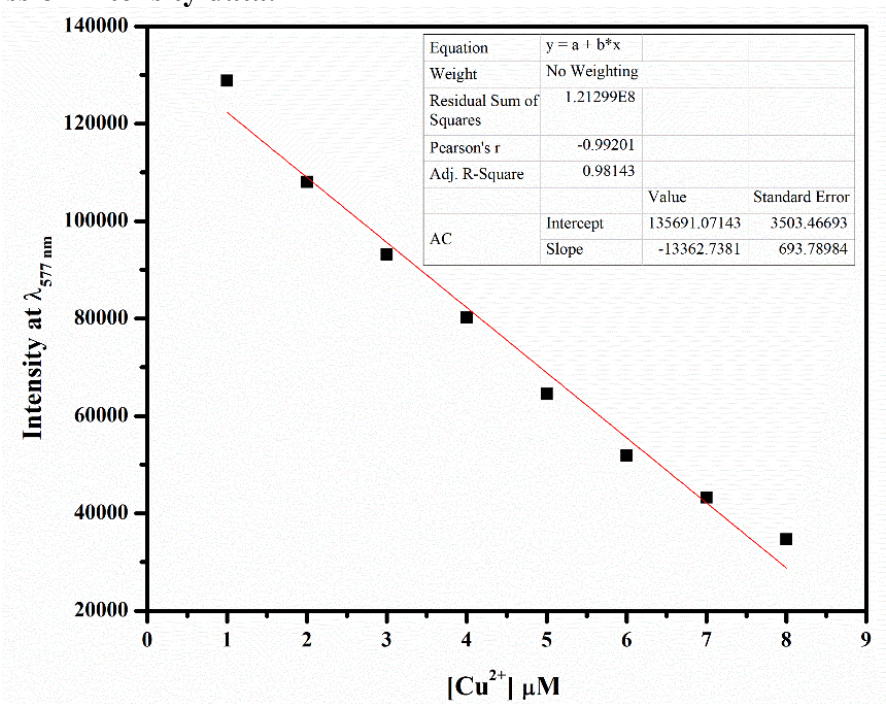

Fig. S31 Plot of Intensity at 577 nm versus concentration of Cu^{2+} and the calculated limit of Detection of ACQ for Cu^{2+} is 0.25 μM

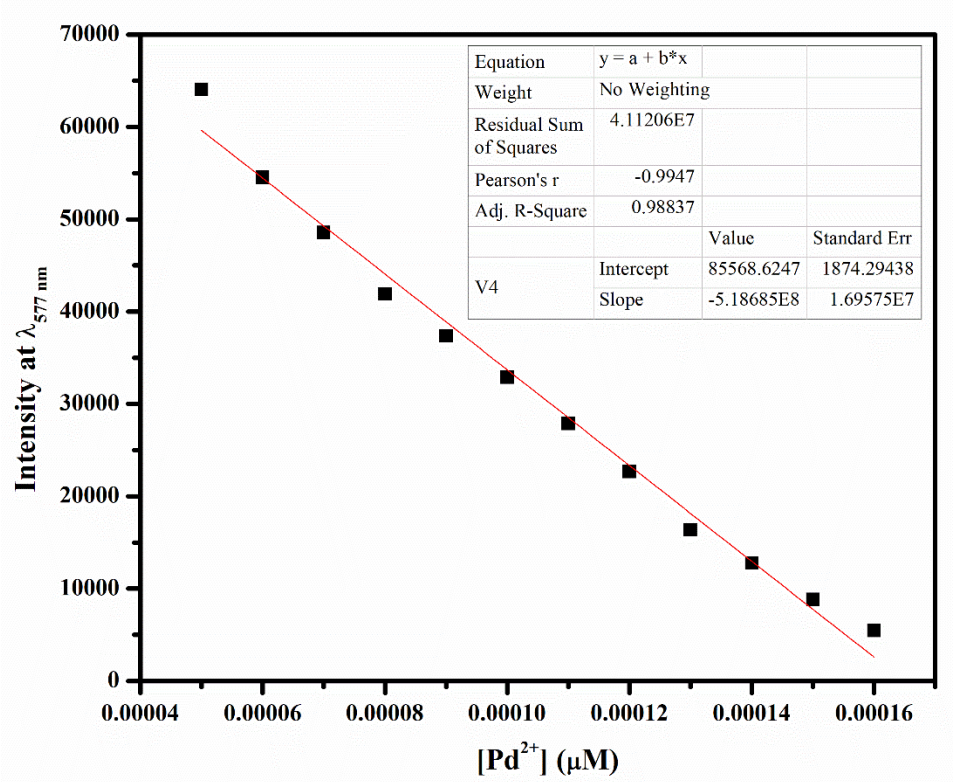

Fig. S32 Plot of Intensity versus concentration of Pd^{2+}at 577 nm and the calculated limit of Detection of ACQ for Pd^{2+} is 11.87 μM

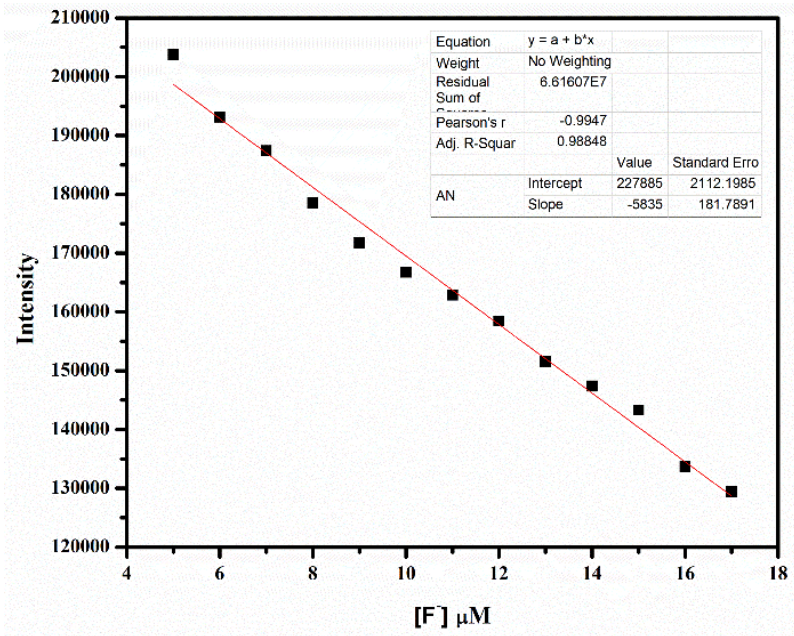

Fig. S33 Plot of Intensity versus concentration of F^- at 598 nm and the calculated limit of Detection of ACQ for F^- is 1.15 μM

4. Quenching Constant

- The Stern–Volmer graph represents the quenching constant (K_{SV}) which was determined from the slope of the following equation:

$$\frac{F_o}{F} = 1 + K_{sv}[\mathbf{M}^{n\pm}]$$

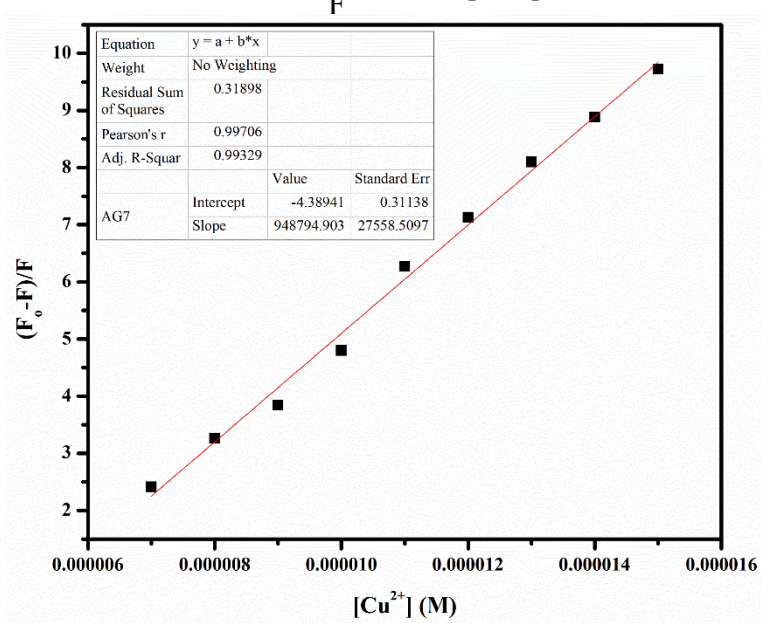

Fig. S34 Stern-Volmer plot for ACQ against varying concentrations of Cu^{2+} in the range of 0-15 μM

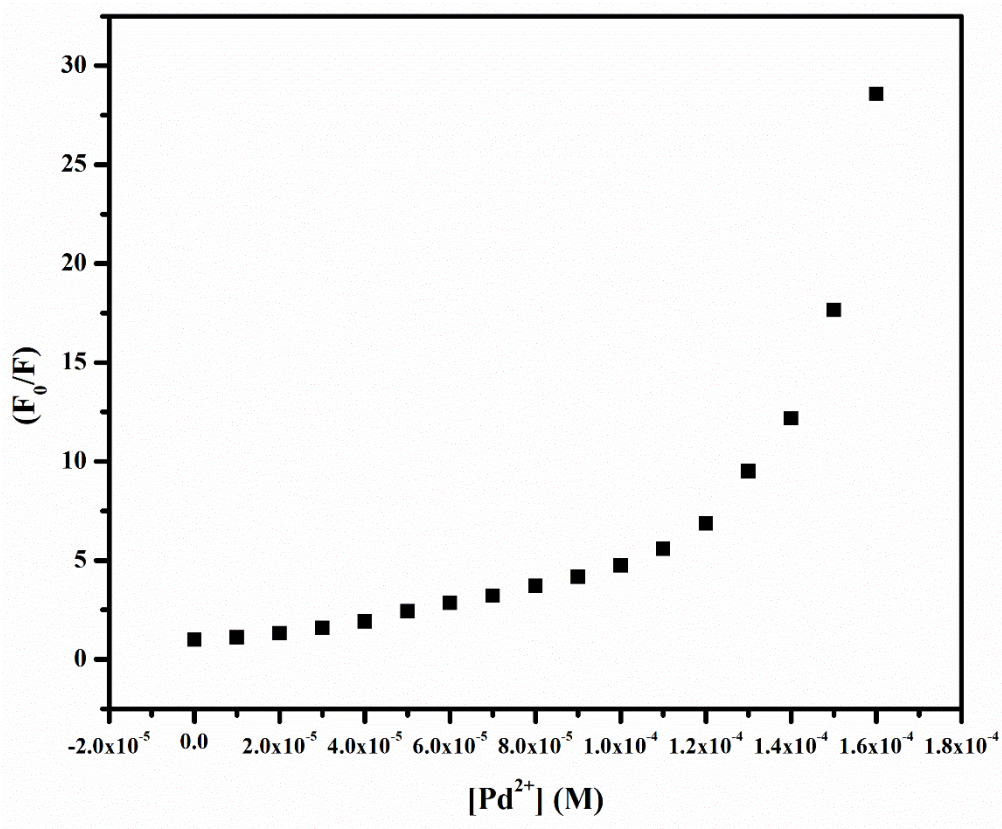

Fig. S35 Fractional fluorescence (F_0/F) versus [Pd^{2+}] plot in the range of 0-180 μM

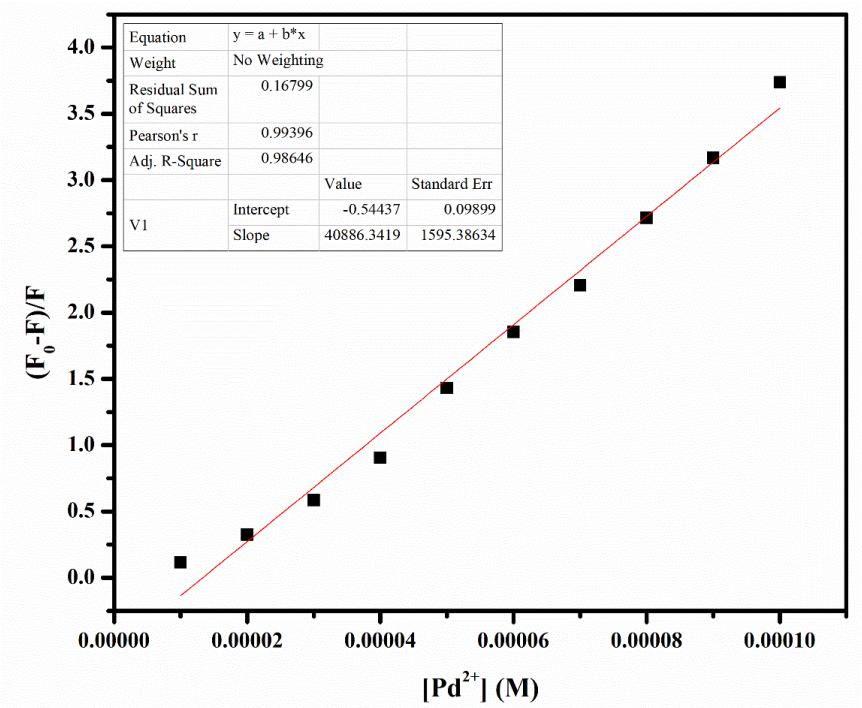

Fig. S36 Stern-Volmer plot for ACQ against varying concentrations of Pd^{2+} in the range of 0-100 μM

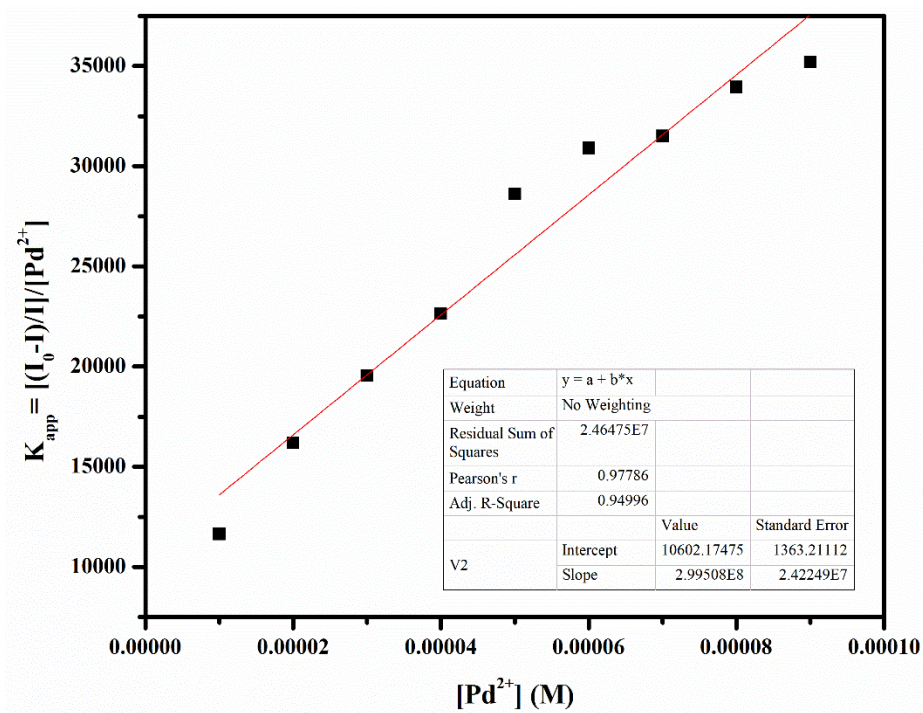

Fig. S37 Plot of K_{app} versus $[Pd]^{2+}$

In case of Pd^{2+}, at higher concentrations quenching occurred due to both complex formation as well as collisional quenching with Pd^{2+}, which is evident from the fractional fluorescence (F_0/F) versus $[Pd^{2+}]$ plot as well as the lifetime measurements where the characteristic upward curvature and the lowering of average lifetime upon increasing the concentration of Pd^{2+} indicated both static and dynamic quenching.

The Static quenching constant (K_{sv}), 2.6 x 10^4 M^{-1} was determined from the Stern-Volmer plot from the low concentration region of Pd^{2+} using the equation

$$\frac{F_o}{F} = 1 + K_{sv}[\mathbf{Pd^{2+}}]$$

While the dynamic quenching constant was obtained from the plot of K_{app} (Apparent Quenching constant) versus $[Pd^{2+}]$ where

$$K_{app} = [\frac{F_o}{F} - 1]\ \frac{1}{[\mathbf{Pd^{2+}}]} = (K_D + K_S) + K_D K_S[\mathbf{Pd^{2+}}]$$

The individual values of K_D and K_S were obtained from straight line with an intercept(I) of K_D + K_S and a slope(S) of $K_D K_S$. Since the value of K_{sv} (or K_S) from the Stern Volmer plot is known, upon solving the quadratic equation $K_S^2 - K_S I + S = 0$,

2.1 x 10^4 M^{-1} was assigned as Static Quenching constant (K_{sv}) and from the formula of Slope(S) the value of Dynamic Quenching constant (K_D) was calculated as 1.3 x 10^4 M^{-1}

Reference used for the calculations

DC Santra, MK Bera, PK Sukul and S Malik, Chem. Eur. J. 2016, 22, 2012 – 2019.

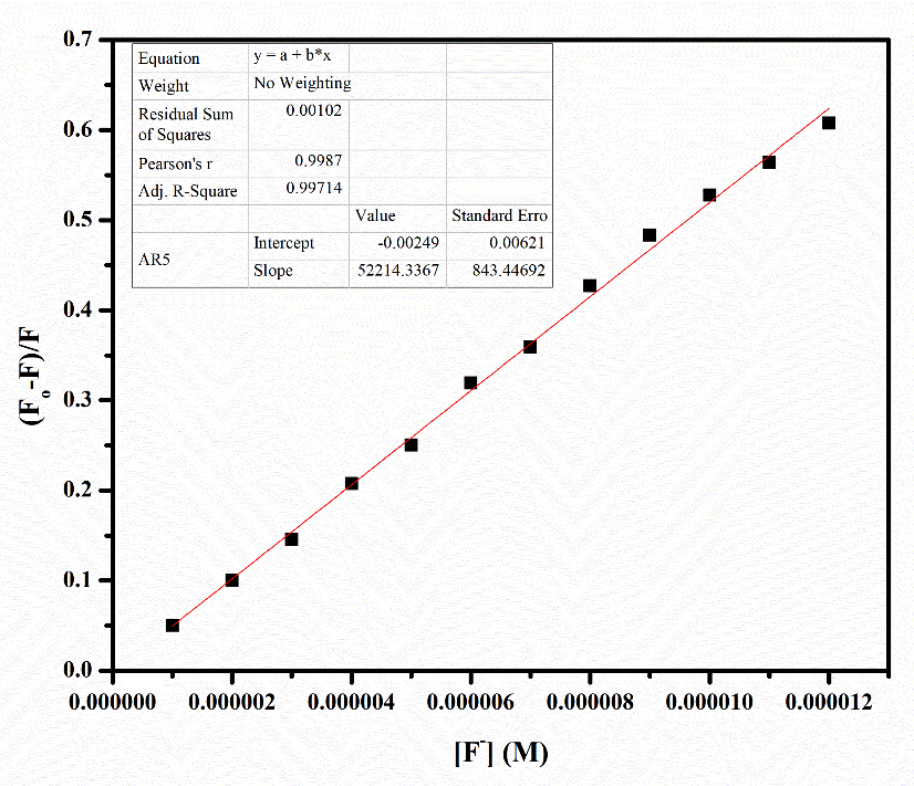

Fig. S38 Stern-Volmer plot for ACQ against varying concentrations of F^- in the range of 0-15 μM

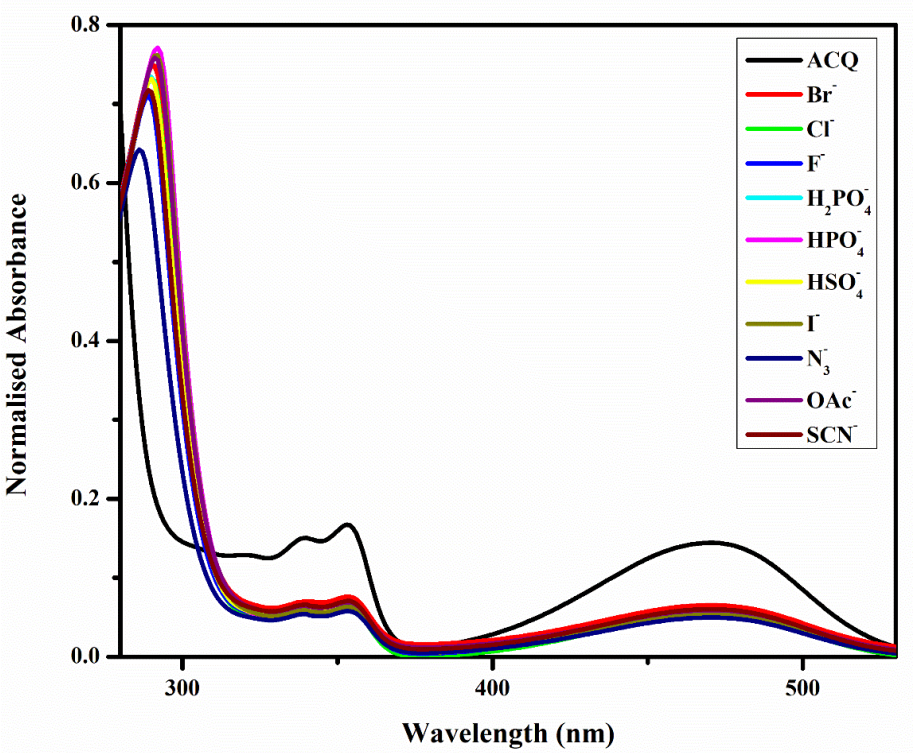

Fig. S39 UV–vis spectra of ACQ (10 μM) in the presence of various anions (50μM) in H_2O

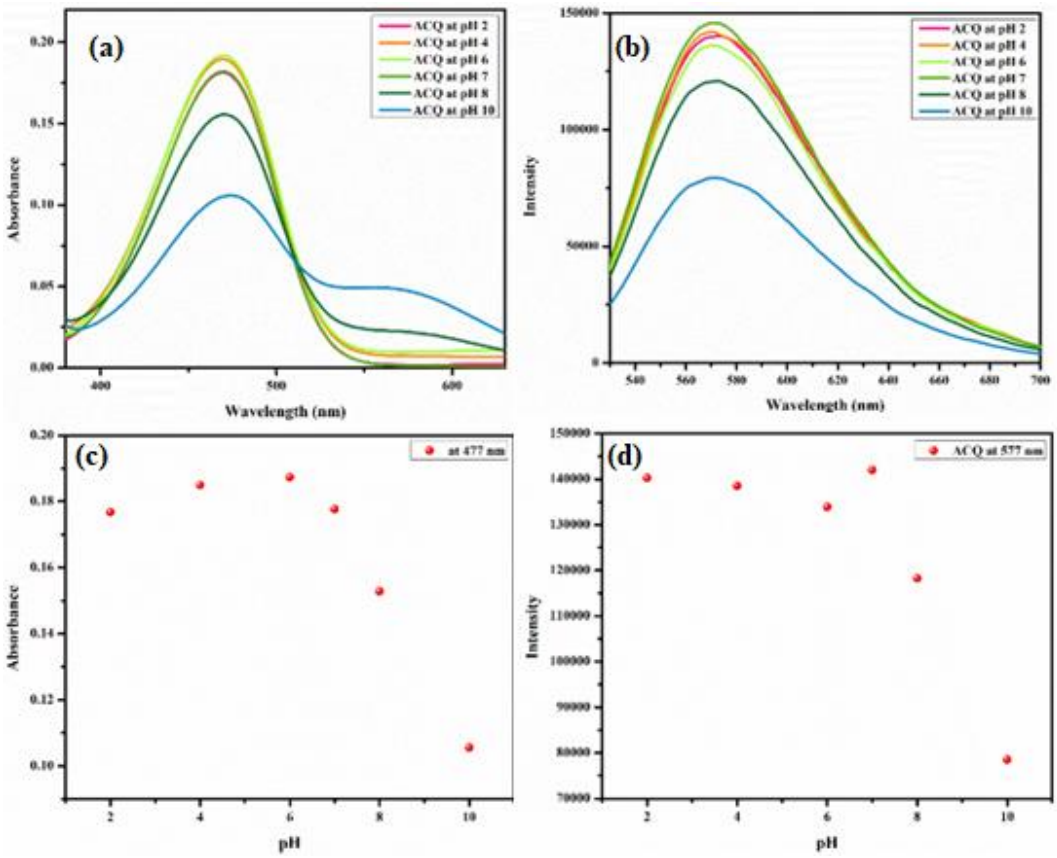

Fig. S40 (a) Absorbance spectra and (b) Emission spectra of ACQ (50μM) at different pH. (c) Scatter plot of Absorbance Vs pH and (d) Intensity vs pH for ACQ (50 μM) at 477 and 577 nm respectively.

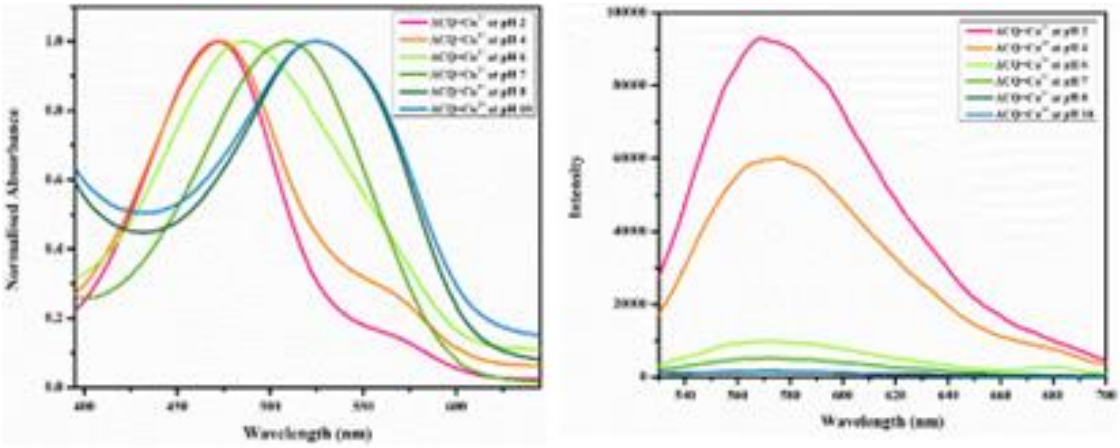

Fig. S41 (a)Normalized Absorbance spectra and (b) Emission spectra of ACQ (50μM) + Cu^{2+} (20μM) at different pH

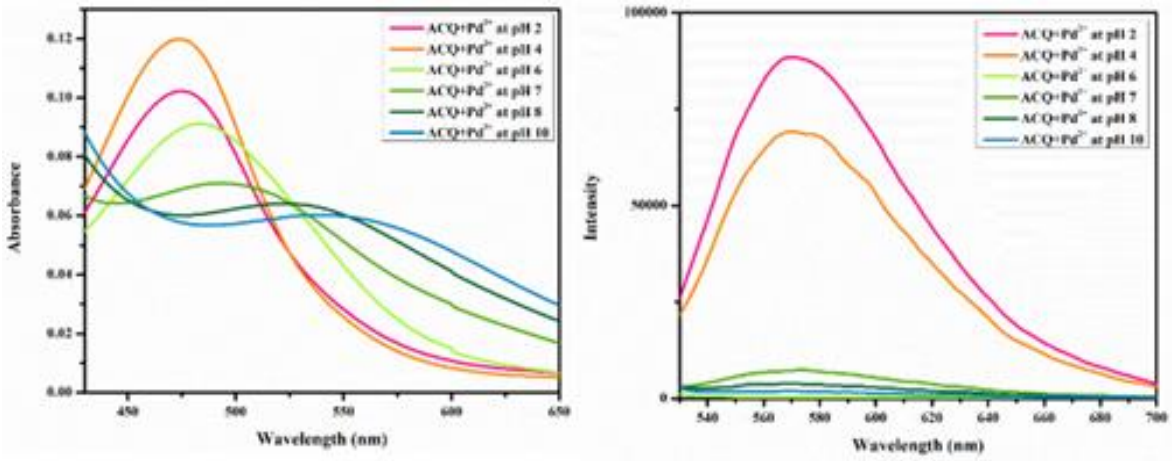

Fig. S42 (a)Absorbance spectra and (b) Emission spectra of ACQ (50μM) + Pd^{2+} (100μM) at different pH

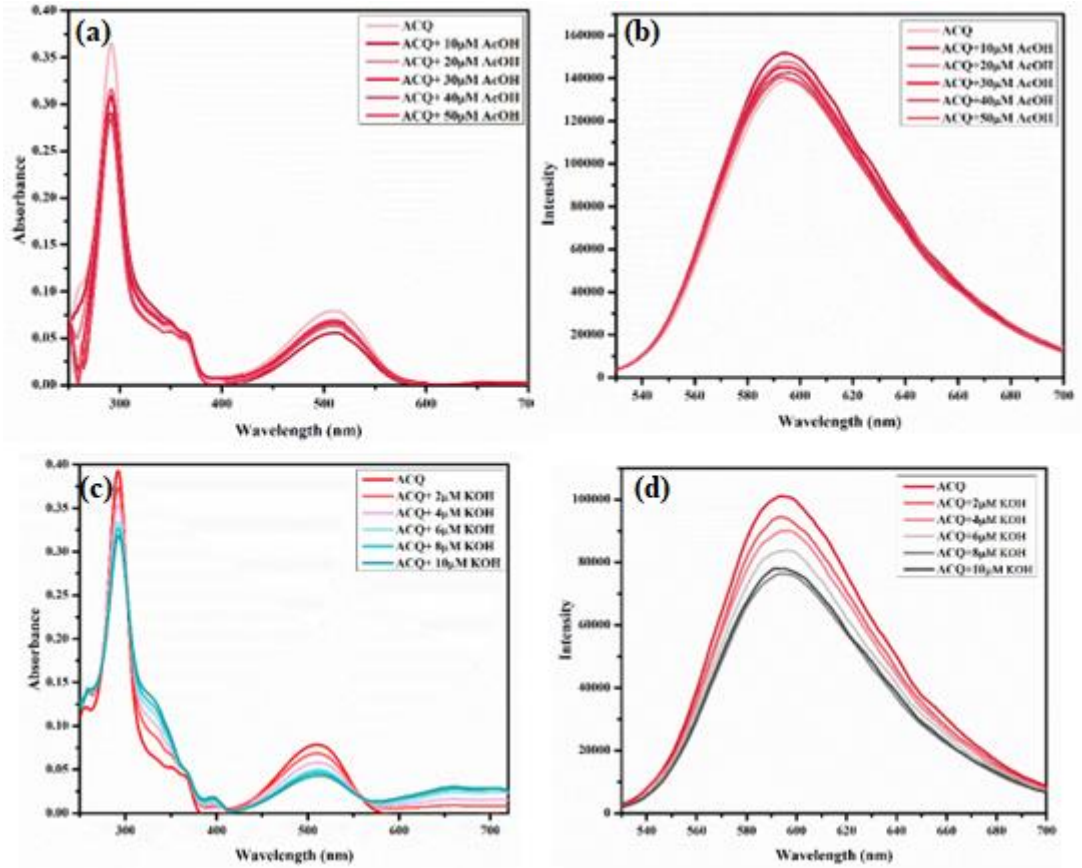

Fig. S43 (a) Absorbance spectra and (b) Emission spectra of ACQ (10μM) with varying concentrations of AcOH (10-50μM) in DMSO (c) Absorbance spectra and (b) Emission spectra of ACQ (10μM) with varying concentrations of KOH (0-10μM) in DMSO

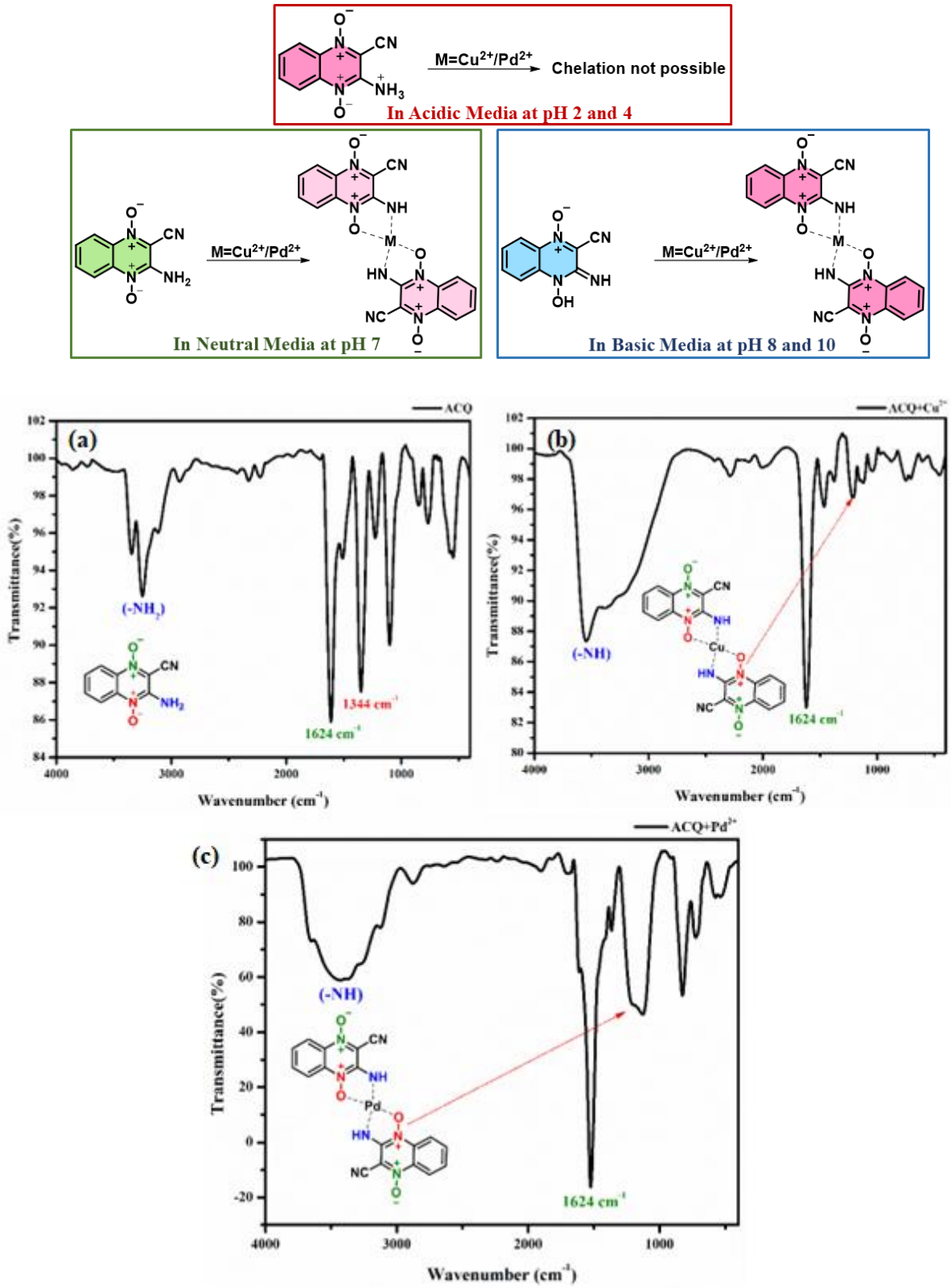

Fig. S44 Plausible structures of ACQ at different pH and FT-IR Spectrum of (a) ACQ (b) ACQ+Cu^{2+} and (c) ACQ+Pd^{2+}

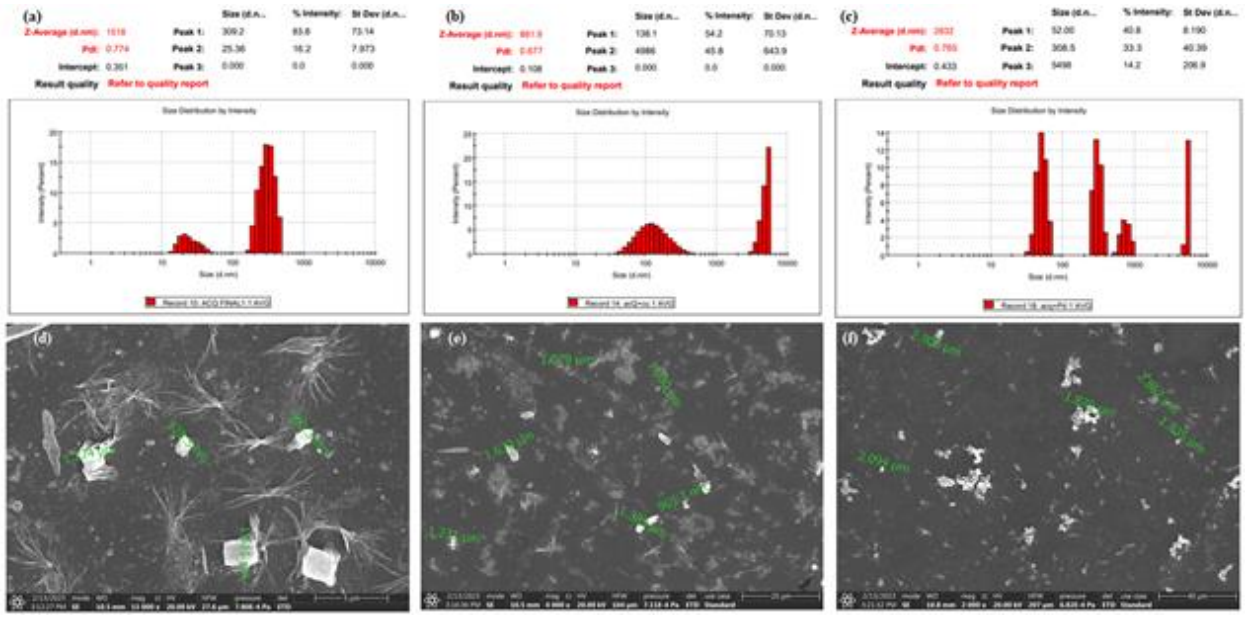

Fig. S45 Particle size histogram of (a) ACQ (b) ACQ+Cu^{2+} (c) ACQ+Pd^{2+} and FE-SEM images of (d) ACQ (e) ACQ+Cu^{2+} (f) ACQ+Pd^{2+}

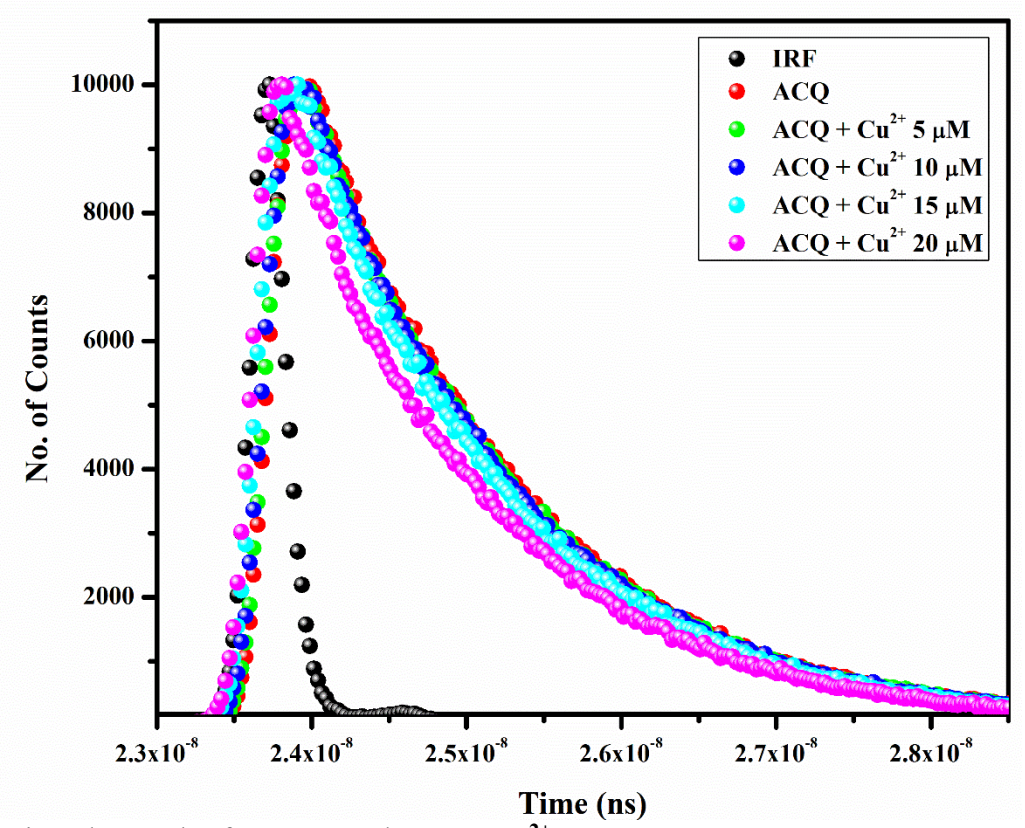

Fig. S46 Time decay plot for **ACQ** and **ACQ+Cu^{2+}**

Sample	Average lifetime (τ)	χ^2
ACQ (10 μM)	1.10 ns	1.03
ACQ (10 μM)+Cu^{2+} (5 μM)	1.09 ns	1.10
ACQ (10 μM)+Cu^{2+} (10 μM)	1.17 ns	1.07
ACQ (10 μM)+Cu^{2+} (15 μM)	1.13 ns	1.17
ACQ (10 μM)+Cu^{2+} (20 μM)	0.82 ns	1.18

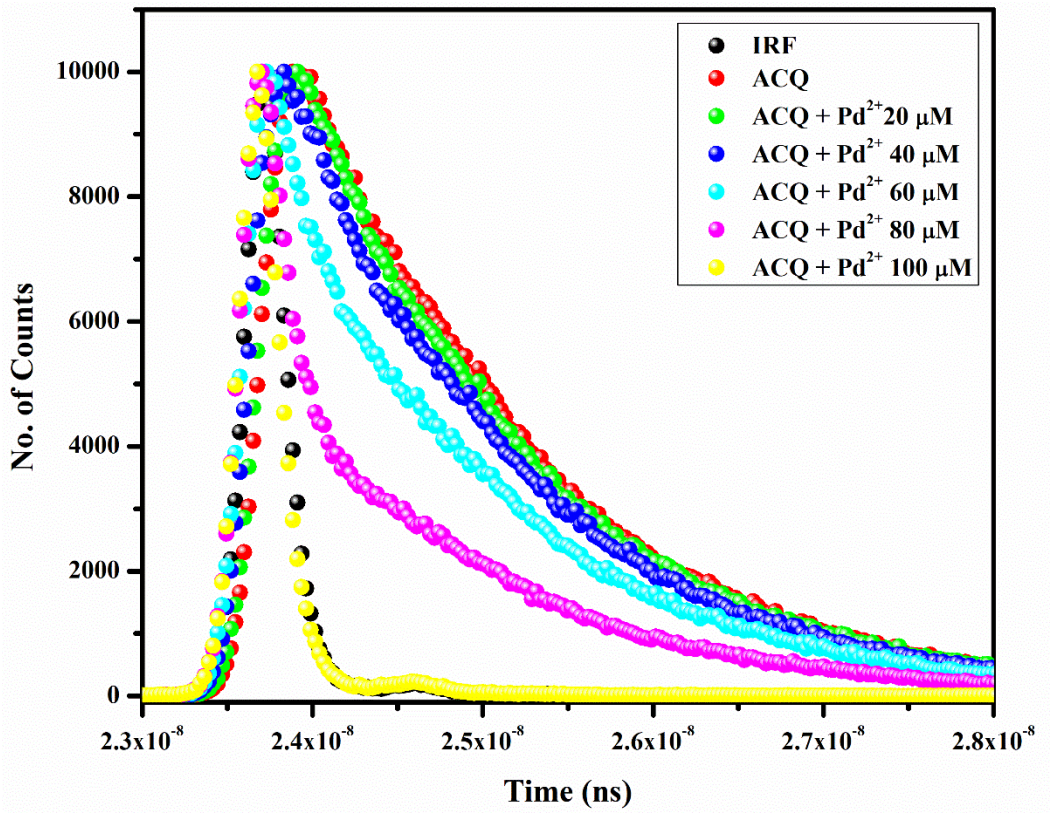

Fig. S47 Time decay plot for **ACQ** and **ACQ+Pd^{2+}**

Sample	Average lifetime (τ)	χ^2
ACQ (10 μM)	1.27 ns	0.99
ACQ (10 μM)+Pd^{2+} (20 μM)	1.18 ns	1.04
ACQ (10 μM)+ Pd^{2+} (40 μM)	0.86 ns	1.03
ACQ (10 μM)+ Pd^{2+} (60μM)	0.21 ns	1.19
ACQ (10 μM)+ Pd^{2+} (80 μM)	0.10 ns	1.03
ACQ (10 μM)+ Pd^{2+} (100 μM)	0.035 ns	0.98

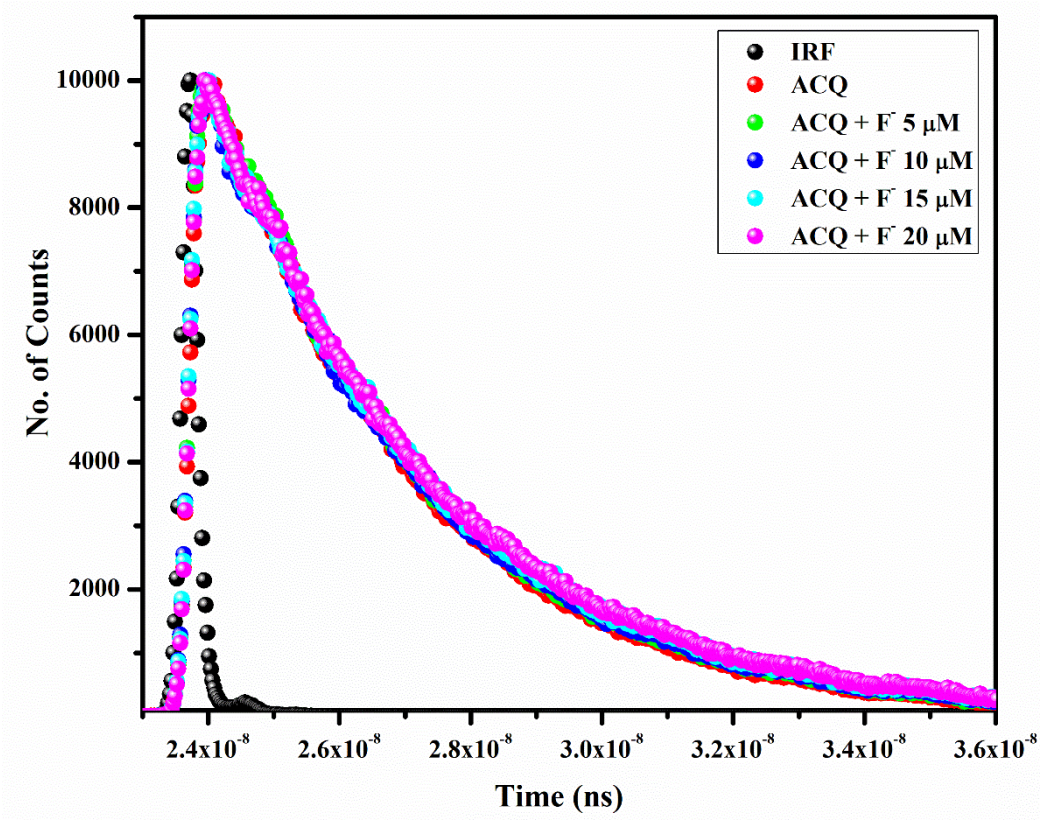

Fig. S48 Time decay plot for **ACQ** and **ACQ+F$^-$**

Sample	Average lifetime (τ)	χ^2
ACQ (10 μM)	3.10 ns	1.16
ACQ (10 μM)+F$^-$ (5 μM)	3.21 ns	1.16
ACQ (10 μM)+ F$^-$ (10 μM)	3.27 ns	1.14
ACQ (10 μM)+ F$^-$ (15 μM)	3.35 ns	1.17
ACQ (10 μM)+ F$^-$ (20 μM)	3.39 ns	1.18

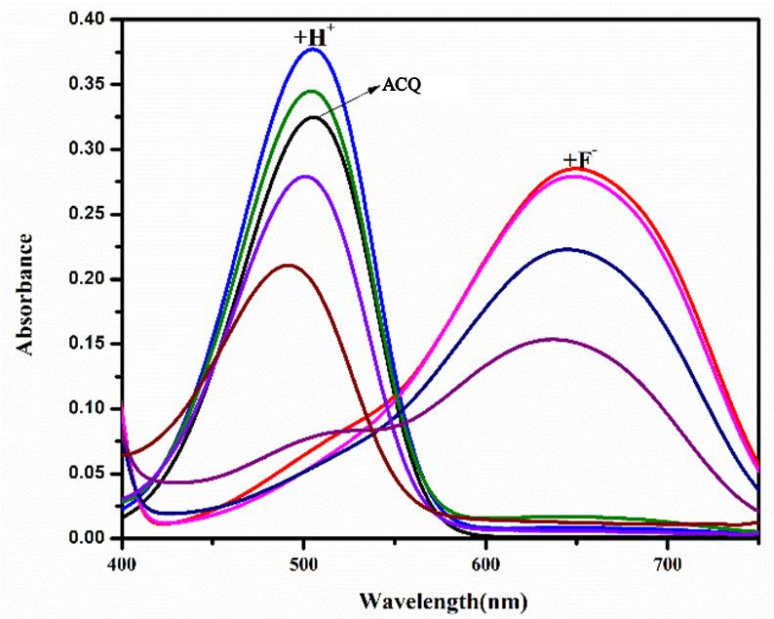

Fig. S49 UV–vis spectra depicting reversibility of ACQ with alternative addition of F^- (656 nm) and AcOH (505 nm).

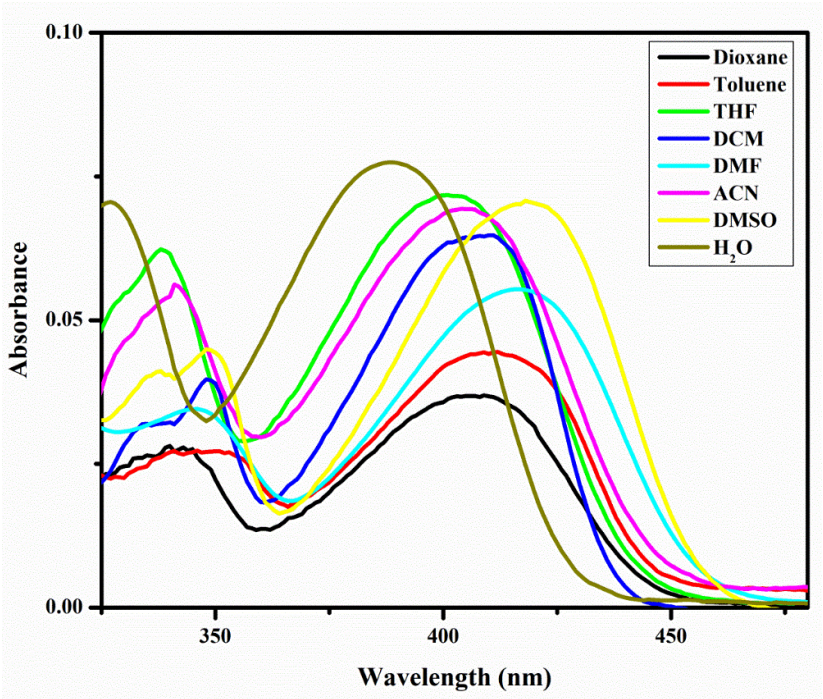

Fig. S50 Absorption spectra in different solvents (10 μM) for AMQ.

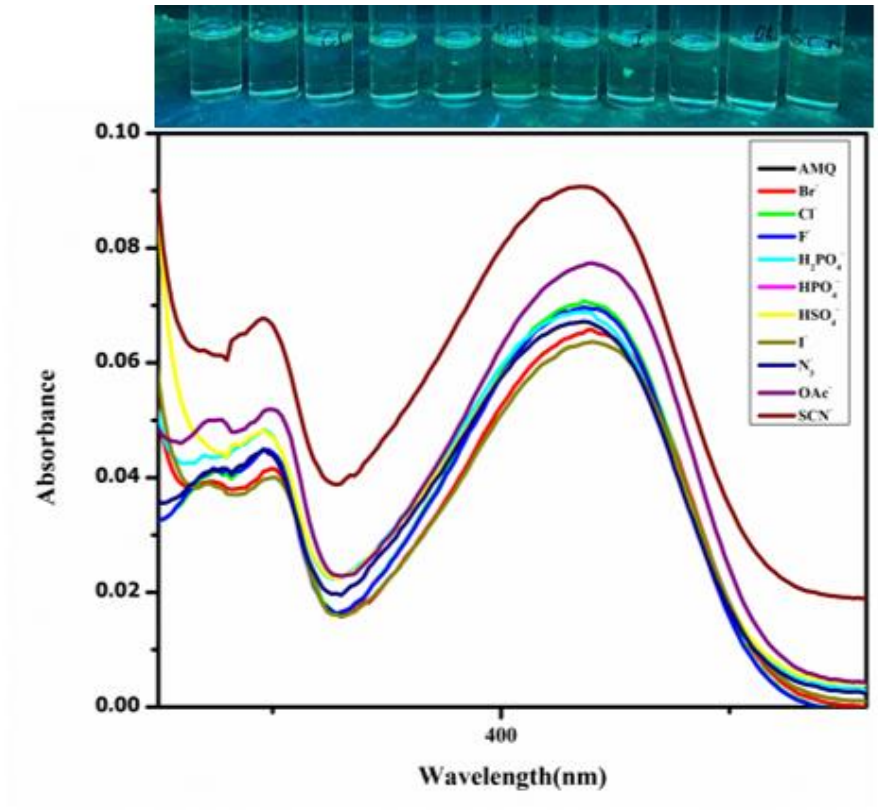

Fig. S51 Absorbance spectra of AMQ (10μM) in the presence of various anions (50μM) in DMSO.

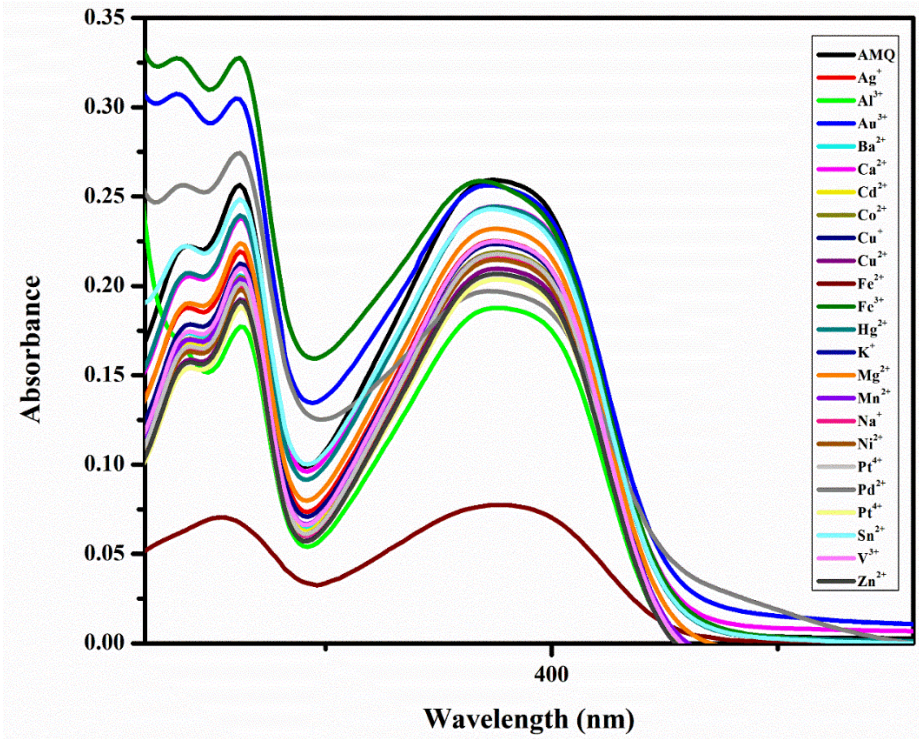

Fig. S52 Absorbance spectra of AMQ (50μM) in the presence of various cations (1mM) in H_2O.

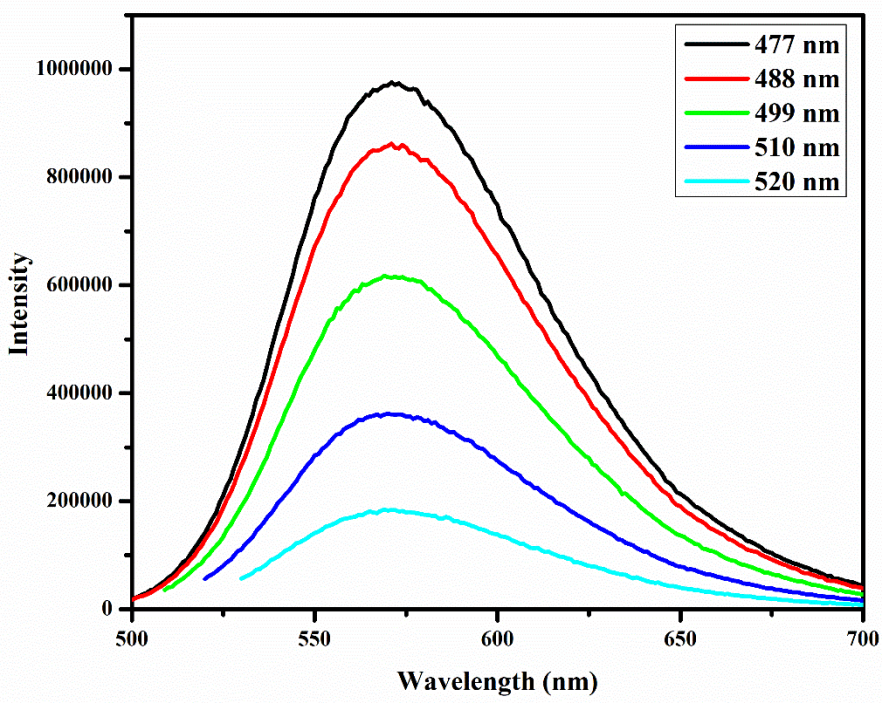

Fig S53. A plot of Intensity versus wavelength for ACQ (10 μM) in H_2O at different Excitation wavelengths.

Cu^{2+} Application

Preparation of artificial urine sample:

250mg urea, 29mg NaCl, 16mg KCl, 22.5mg Na_2SO_4, 14mg KH_2PO_4, 11mg creatinine, 10mg NH_4Cl and 11mg $CaCl_2 \cdot H_2O$ were dissolved in 10ml millipore water. [30]

Experimental Protocol:

20μL of the artificial urine solution in 2ml water was titrated by adding different concentrations of Cu^{2+} (2-8 μM for recording absorbance data and 0-4 μM for obtaining Intensity versus concentration of Cu^{2+} plot)

The values of slope (m= 0.00585) and intercept (c=0.02084) were taken from absorbance versus [Cu^{2+}] calibration plot **(Fig. S49)**.

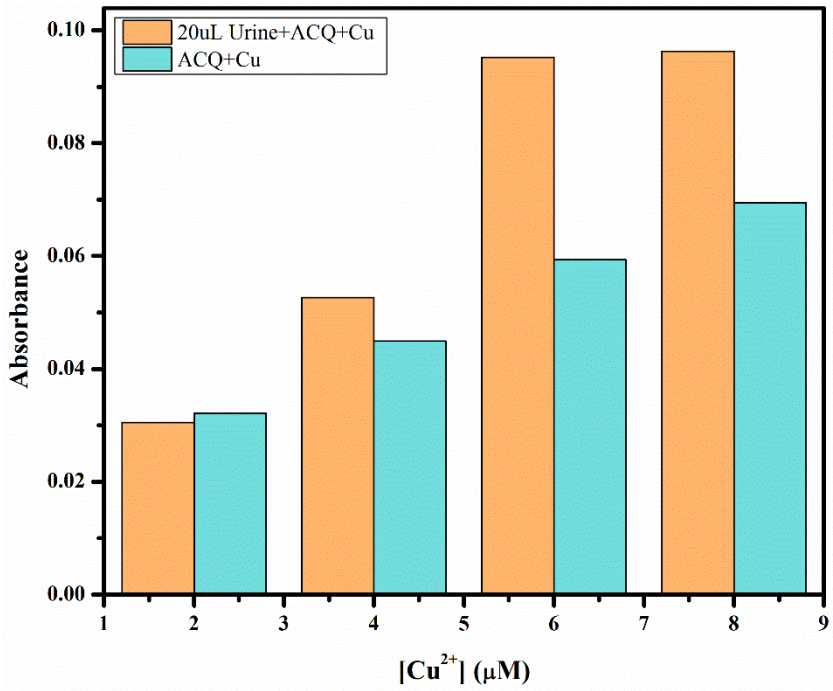

Fig. S54 Bar graph for ACQ at 527nm obtained by titrating 20 μL samples of artificial urine with Cu^{2+}(2-8 μM) in H_2O.

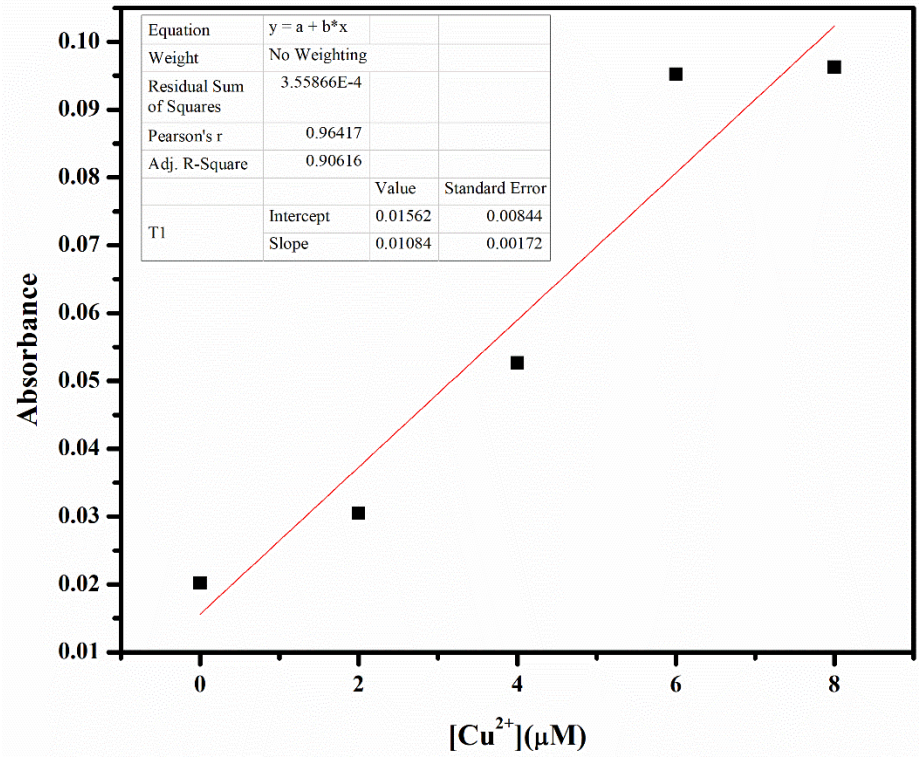

Fig.S55 Absorbance versus [Cu^{2+}] plot for ACQ+20μL artificial urine at different concentrations (2-8 μM) of Cu^{2+} in H_2O.

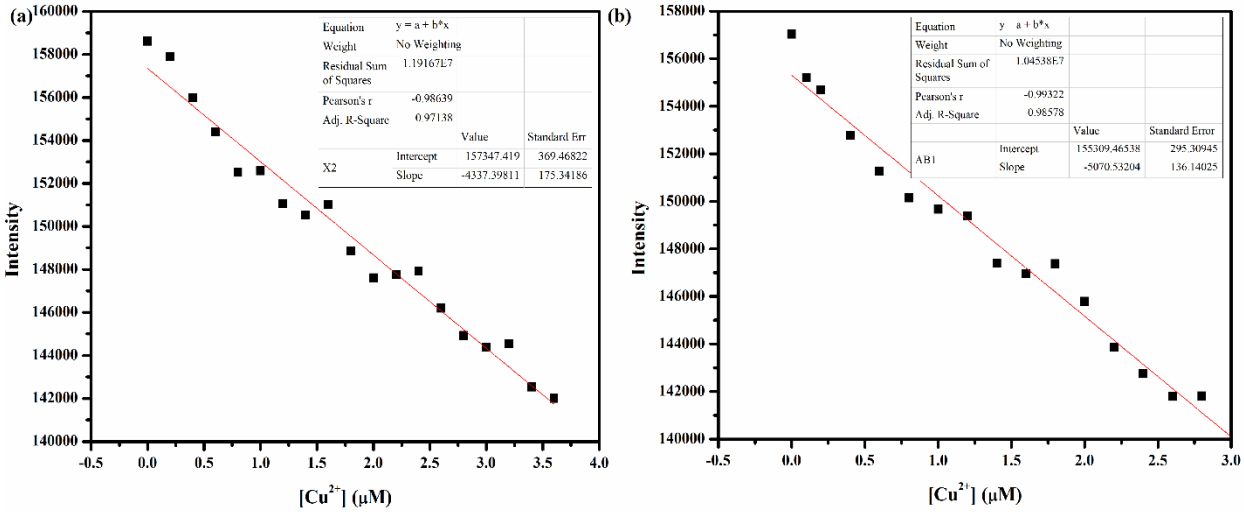

Fig.S56 Intensity versus [Cu^{2+}] plot for (a) ACQ (b) and 20μL with different concentrations (0-3 μM) of Cu^{2+} at 527 nm in H_2O.

Remarks: This experiment is performed to demonstrate the utility of probe ACQ in the quantitative detection of Cu^{2+} present in the urine of Wilson's disease patients and to show its potential for clinical applications. Even in the presence of all the components present in the urine sample the probe can efficiently be utilized for quantifying Cu^{2+} in Wilson's disease patients by using the above method.

Pd^{2+} Application

Experimental Protocol:

50 mg of all four drug samples Avomine, Dolo 650 and Meftal were dissolved in 3ml water and the solution was filtered. 2μL was taken from each of the solutions and titrated with Pd^{2+} (20-100 μM) and the obtained absorbances at the respective concentrations were tabulated and the corresponding bar graph was plotted.

Inference: After adding the drug samples along with the probe in water no peak at 527 nm was observed in UV. No Pd^{2+} was found in any of the drug samples as indicated by the bar graph. However, after titrating the samples with Pd^{2+} salt (0-40 μM) which showed a gradual increase in absorbance at 527 nm which indicated that the concentration of Pd^{2+} in the drug samples was below the detection limit of ACQ and the limit allowable for a Pd^{2+} in drug

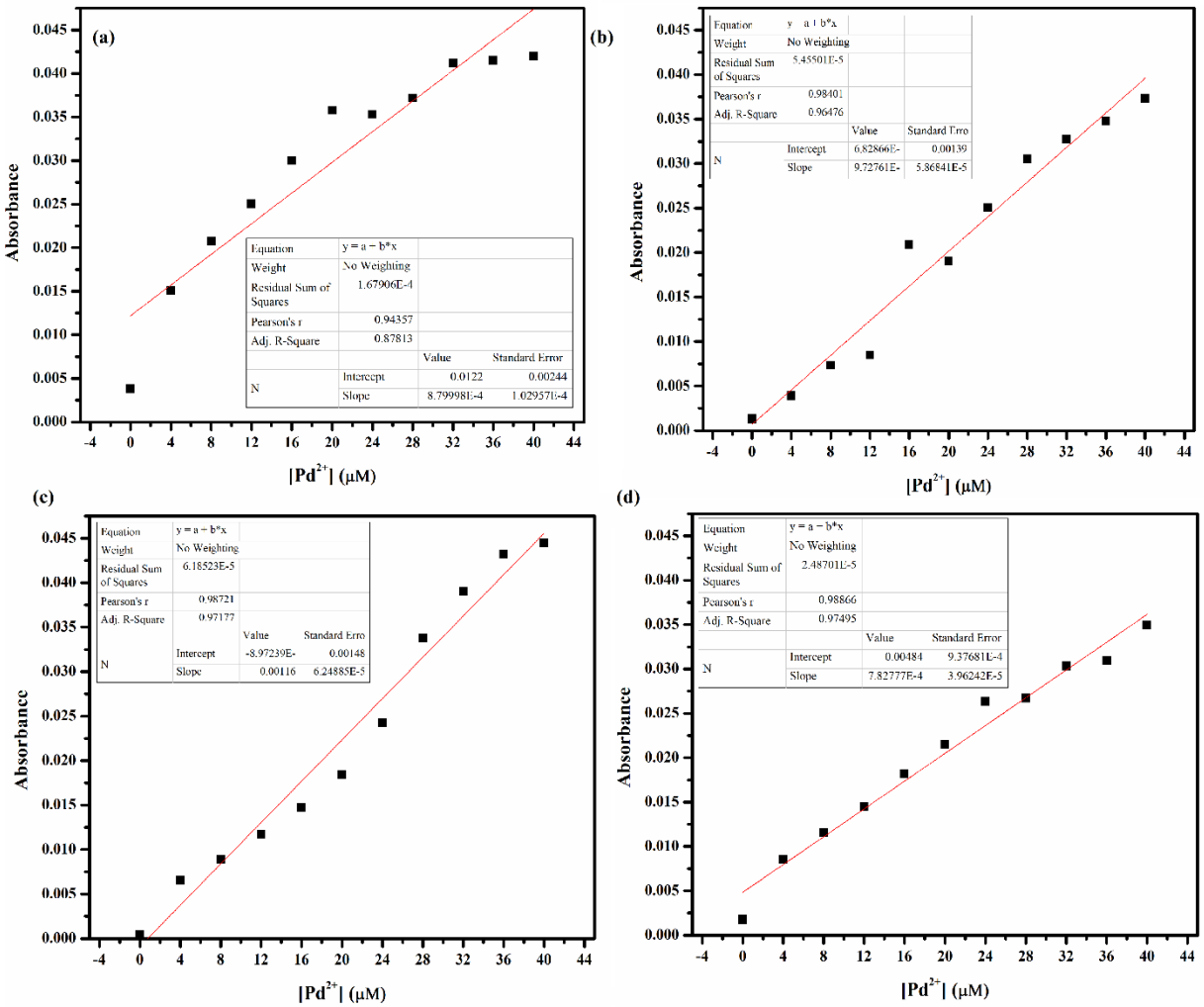

Fig S57. Scatter plots for (a)ACQ with Pd^{2+}(0-40 μM) along with (b) Avomine (c) Dolo 650 and (d) Meftal at 527 nm in H_2O.

Table S4. Absorbance values at 527 nm for various drug samples.

	Absorbance			
[Pd^{2+}]	**Avomine+ ACQ+Pd^{2+}**	**Dolo 650+ ACQ+Pd^{2+}**	**Meftal+ ACQ+Pd^{2+}**	**ACQ+Pd^{2+}**
4 μM	0.00394	0.00654	0.00854	0.0151
8 μM	0.00733	0.00893	0.01159	0.02078
12 μM	0.00851	0.01169	0.01448	0.02508
16 μM	0.02093	0.01471	0.0182	0.03003
20 μM	0.01906	0.01844	0.02149	0.03582
24 μM	0.02505	0.02428	0.02634	0.03529
28 μM	0.03054	0.03376	0.02674	0.03718
32 μM	0.03272	0.03904	0.03034	0.04119

36 μM	0.03476	0.04324	0.03097	0.04154
40 μM	0.03738	0.04448	0.03494	0.04199

F^- Application

Experimental Protocol:

100 mg of toothpaste samples Colgate, Pepsodent and Sensodyne were weighed and dissolved in 5 ml DMSO.

10μL of the solution in 2ml DMSO was titrated by adding different concentrations of F^- (2-8 μM) and the obtained values were used to determine the concentration of fluoride by using the equation

$$\mathbf{x = \frac{y - c}{m}}$$

The values of slope (m= 0.00397) and intercept (c=0.01349) were taken from absorbance versus [F^-] calibration plot **(Fig. S52)**.

Remarks: The outcomes obtained indicate that **ACQ** is potentially useful for the quantification of F in toothpaste samples. The amount of fluoride recovered in each of the samples is tabulated below **(Table S5)**.

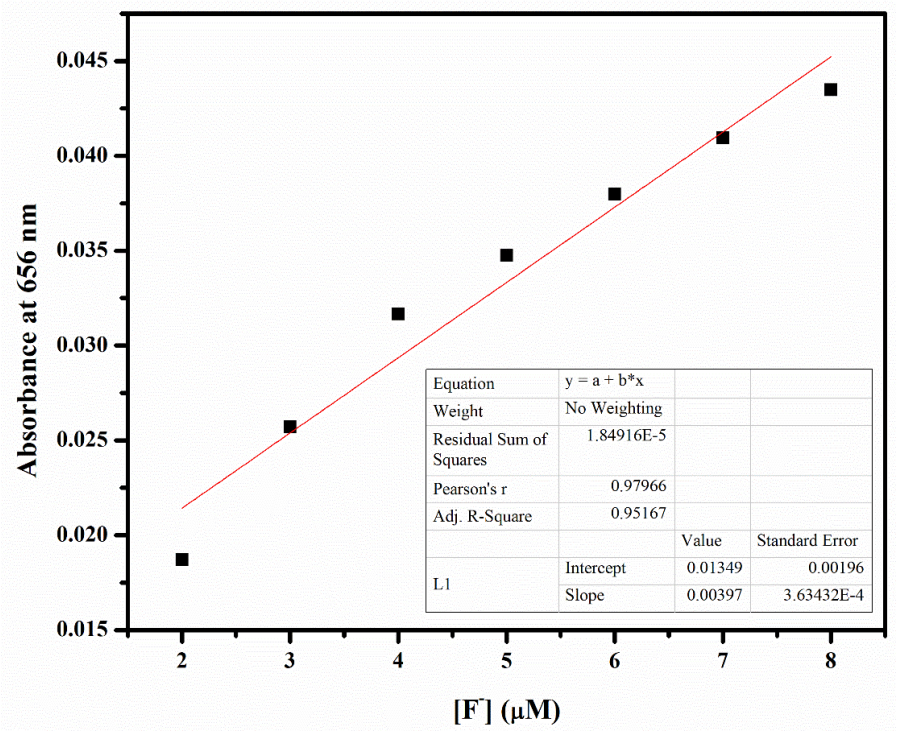

Fig S58. Absorbance versus [F^-] plot for ACQ at different concentrations of F^- in DMSO.

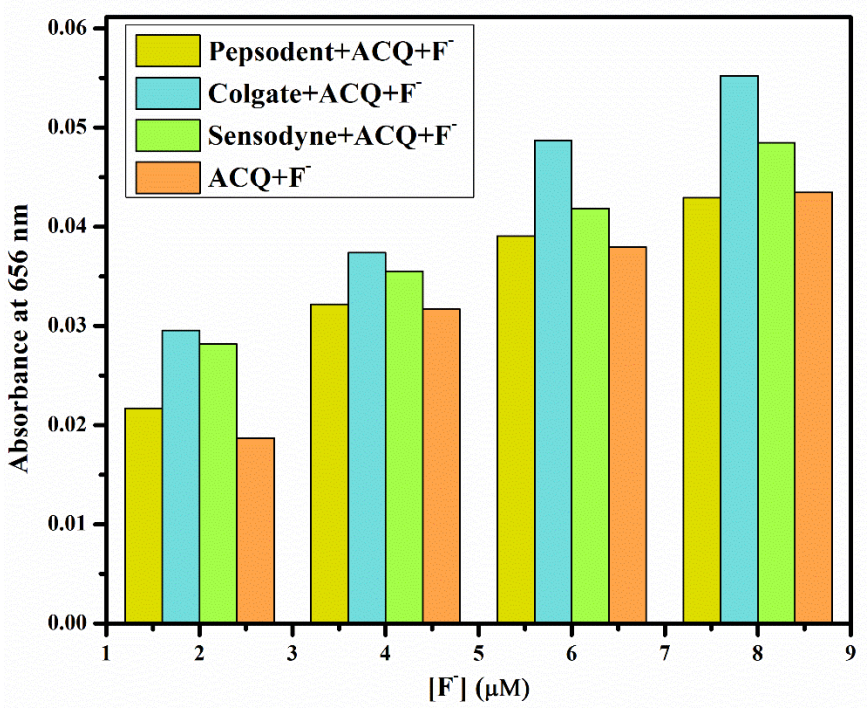

Fig S59. Bar graph for ACQ at 656 nm obtained by titrating toothpaste samples with F^-(2-8 μM) in DMSO.

Table S5. Calculated parameters from the obtained experimental values for quantifying F^- in different toothpaste samples.

Absorbance of ACQ+F^- at z	[F^-] (z)	Absorbance of Colgate +ACQ+ [F^-] (z)	$x_{colgate}$	Concentration found in Sample ($x_{colgate}$-z)
0.01871	2 μM	0.02956	4.04 μM	2.04μM
0.03168	4 μM	0.0374	6.02 μM	2.02 μM
0.03798	6 μM	0.0487	8.87 μM	2.86 μM
0.04348	8 μM	0.05521	10.5 μM	2.50 μM

Absorbance of ACQ+F^- at z	[F^-] (z)	Absorbance of Pepsodent +ACQ+ [F^-] (z)	$x_{pepsodent}$	Concentration found in Sample ($x_{pepsodent}$-z)
0.01871	2 μM	0.0217	2.0689	0.068 μM
0.03168	4 μM	0.0322	4.7128	0.71 μM
0.03798	6 μM	0.03907	6.4433	0.44 μM
0.04348	8 μM	0.04293	7.415	-0.59 μM

Absorbance of ACQ+F^- at z	[F^-] (z)	Absorbance of Sensodyne +ACQ+ [F^-] (z)	$x_{sensohyde}$	Concentration found in Sample ($x_{sensodyne}$-z)
0.01871	2 μM	0.02818	3.7002	1.70 μM
0.03168	4 μM	0.03551	5.546	1.54 μM
0.03798	6 μM	0.04183	7.138	1.13 μM
0.04348	8 μM	0.04846	8.8085	0.80 μM

Table. S6 Examples of previously reported colorimetric and fluorescence-based Cu^{2+}sensors

Sensor	Detection Limit	Solvent	Reference
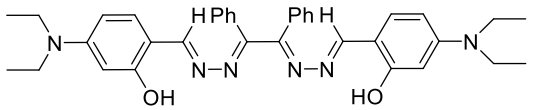	0.73 nM	MeOH/ H_2O	[10]
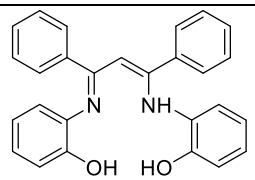	-	MeOH	[11]
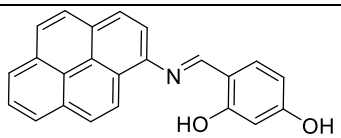	0.503 μM	MeCN/ H_2O	[12]
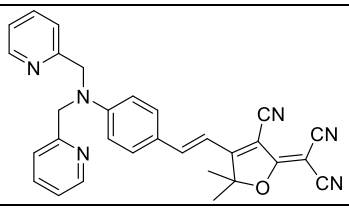	0.102 μM	EtOH/HEPES buffer	[13]
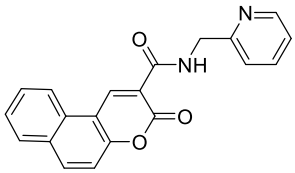	-	DNF/ HEPES buffer	[14]
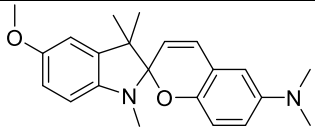	0.11 μM	EtOH	[15]
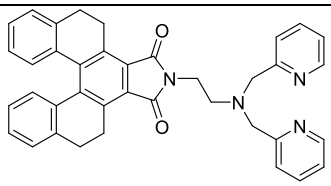	5.6 ppb	HEPES buffer	[16]

Table S7 Examples of previously reported colorimetric and fluorescence-based Pd^{2+}sensors

Sensor	Detection Limit	Solvent	Reference
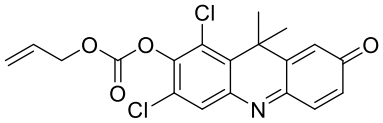	2.2 nM	PBS buffer & DMSO	[17]

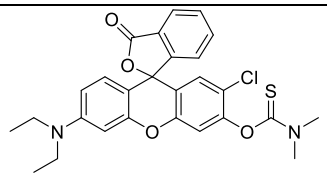	0.01 μM	DMSO	[18]
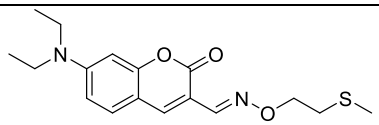	41.5 nM	EtOH/H_2O	[19]
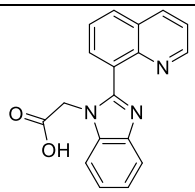	0.26 μM	PBS buffer & DMSO	[20]
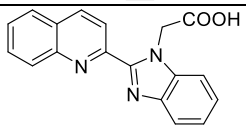	0.089 μM	H_2O	[21]
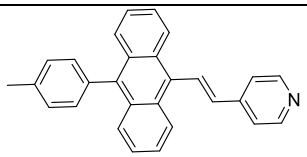	10 ppb	Tween-20 neutral micellar medium	[22]

Table S8 Examples of previously reported colorimetric and fluorescence-based F^- sensors.

Sensor	Detection Limit	Solvent	Mechanism	Reference
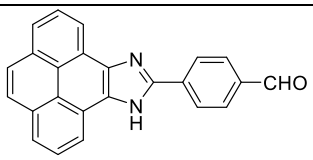	-	DMSO Acetone	ICT Hydrogen Bonding	[1]
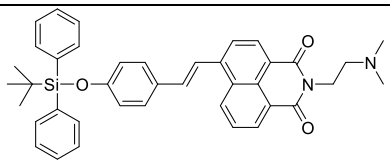	5.27 μM	DMSO	Desilylation	[2]
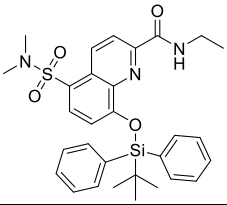	3.8 μM	Dioxane	Desilylation	[3]
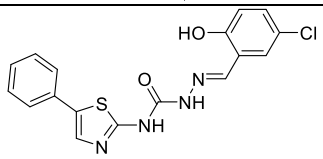	8.6 nM	THF	hydrogen-bonding interactions followed by deprotonation	[4]

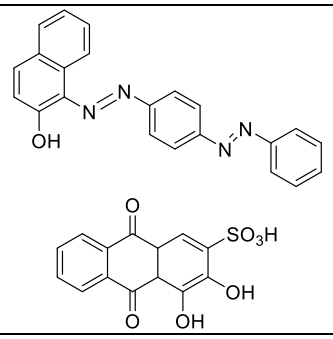	-	-	Deprotonation	[5]
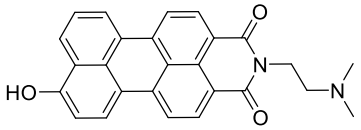	0.495 μM	THF	Deprotonation	[6]
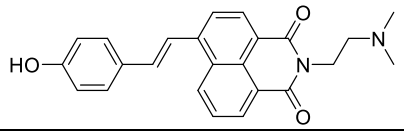	14.2 μM	DMSO	Deprotonation	[7]
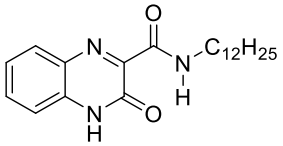	-	THF	ESIPT inhibition	[8]
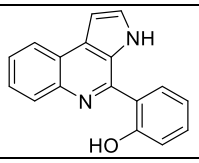	19 μM	THF	Dianion (ICT)	[9]

Table S9 Examples of previously reported molecules with N-oxide group used for fluorescence studies.

Sensor	Reference
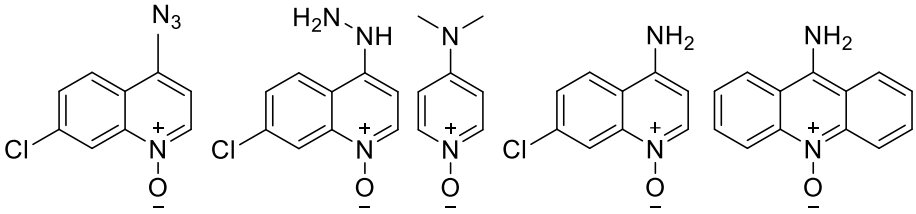	[23]
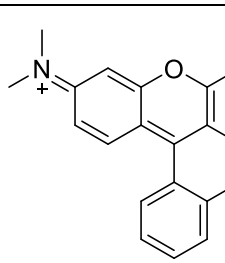	[24]

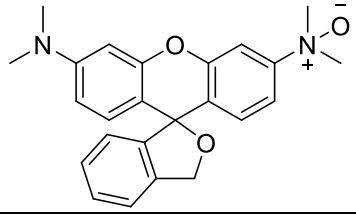	[25]
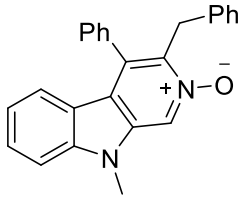	[26]
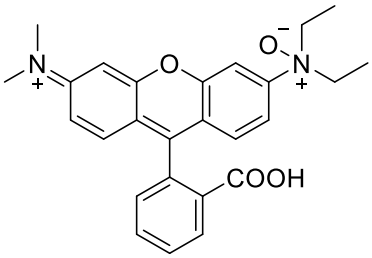 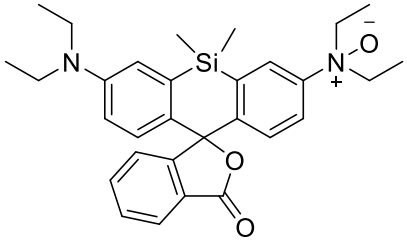 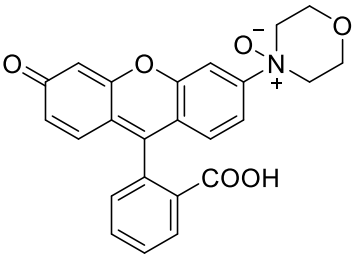 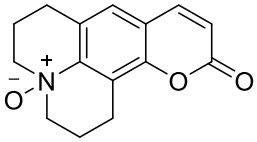	[27]
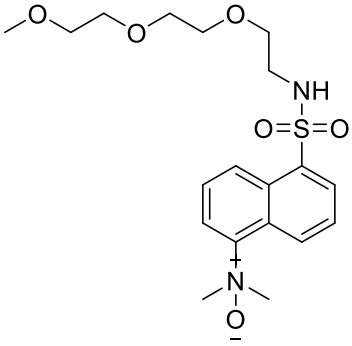	[28]
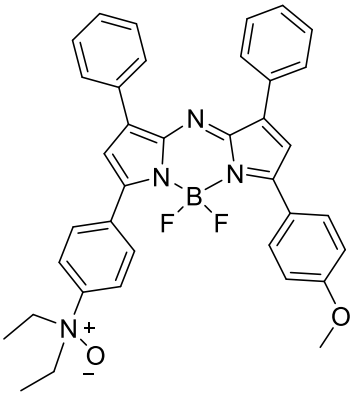	[29]

References:

1. Tabasi, Z. A., Younes, E. A., Walsh, J. C., Thompson, D. W., Bodwell, G. J., & Zhao, Y. (2018). Pyrenoimidazolyl-benzaldehyde fluorophores: synthesis, properties, and sensing function for fluoride anions. ACS omega, 3(11), 16387-16397.
2. Zheng, X., Zhu, W., Ai, H., Huang, Y., & Lu, Z. (2016). A rapid response colorimetric and ratiometric fluorescent sensor for detecting fluoride ion, and its application in real sample analysis. Tetrahedron Letters, 57(52), 5846-5849.
3. Zhou, X., Lai, R., Li, H., & Stains, C. I. (2015). The 8-silyloxyquinoline scaffold as a versatile platform for the sensitive detection of aqueous fluoride. Analytical chemistry, 87(8), 4081-4086.
4. Mondal, S., Gupta, P., Rahaman, F., Gautam, P., & Lekshmi, I. C. (2022). Colorimetric and fluorimetric detection of fluoride ion using thiazole derived receptor. Spectrochimica Acta Part A: Molecular and Biomolecular Spectroscopy, 264, 120301.
5. Kumar, P., Sakla, R., Ghosh, A., & Jose, D. A. (2017). Reversible colorimetric sensor for moisture detection in organic solvents and application in inkless writing. ACS applied materials & interfaces, 9(30), 25600-25605.
6. Mu, M., Ke, X., Cheng, W., Li, J., Ji, C., & Yin, M. (2022). Perylenemonoimide-Based Colorimetric Probe with High Contrast for Naked-Eye Detection of Fluoride Ions. Analytical Chemistry, 94(33), 11470-11475.
7. Zheng, X., Zhu, W., Liu, D., Ai, H., Huang, Y., & Lu, Z. (2014). Highly selective colorimetric/fluorometric dual-channel fluoride ion probe, and its capability of differentiating cancer cells. ACS applied materials & interfaces, 6(11), 7996-8000.
8. Nakane, Y., Takeda, T., Hoshino, N., Sakai, K. I., & Akutagawa, T. (2015). Cation–anion dual sensing of a fluorescent quinoxalinone derivative using lactam–lactim tautomerism. The Journal of Physical Chemistry A, 119(24), 6223-6231.
9. Akula, M., Thigulla, Y., Nag, A., & Bhattacharya, A. (2015). Selective detection of fluoride using fused quinoline systems: effect of pyrrole. RSC advances, 5(70), 57231-57234.
10. Chandra, R., Ghorai, A., & Patra, G. K. (2018). A simple benzildihydrazone derived colorimetric and fluorescent 'on–off-on'sensor for sequential detection of copper (II) and cyanide ions in aqueous solution. Sensors and Actuators B: Chemical, 255, 701-711.
11. Mergu, N., & Gupta, V. K. (2015). A novel colorimetric detection probe for copper (II) ions based on a Schiff base. Sensors and actuators B: Chemical, 210, 408-417.
12. Dalbera, S., Kulovi, S., & Dalai, S. (2018). Pyrene-based Schiff Base as Selective Chemosensor for Copper (II) and Sulfide Ions. ChemistrySelect, 3(23), 6561-6569.
13. Chen, D., Chen, P., Zong, L., Sun, Y., Liu, G., Yu, X., & Qin, J. (2017). Colorimetric and fluorescent probes for real-time naked eye sensing of copper ion in solution and on paper substrate. Royal Society open science, 4(11), 171161.
14. Wang, Y., Feng, H., Li, H., Yang, X., Jia, H., Kang, W., ... & Zhang, R. (2020). A Copper (II) Ensemble-Based Fluorescence Chemosensor and Its Application in the 'Naked–Eye'Detection of Biothiols in Human Urine. Sensors, 20(5), 1331.
15. Trevino, K. M., Tautges, B. K., Kapre, R., Franco Jr, F. C., Or, V. W., Balmond, E. I., ... & Louie, A. Y. (2021). Highly sensitive and selective spiropyran-based sensor for Copper (II) quantification. ACS omega, 6(16), 10776-10789.
16. Sakunkaewkasem, S., Petdum, A., Panchan, W., Sirirak, J., Charoenpanich, A., Sooksimuang, T., & Wanichacheva, N. (2018). Dual-analyte fluorescent sensor based on [5] helicene derivative with super large stokes shift for the selective determinations of Cu2+ or Zn2+ in buffer solutions

and its application in a living cell. ACS sensors, 3(5), 1016-1023.
17. Xia, Q., Feng, S., Liu, D., & Feng, G. (2018). A highly selective and sensitive colorimetric and near-infrared fluorescent turn-on probe for rapid detection of palladium in drugs and living cells. Sensors and Actuators B: Chemical, 258, 98-104.
18. Choi, M. G., Seo, J. Y., Cho, E. J., & Chang, S. K. (2022). Colorimetric analysis of palladium using thiocarbamate hydrolysis and its application for detecting residual palladium in drugs. Journal of Photochemistry and Photobiology A: Chemistry, 429, 113920.
19. Chen, X., Wang, H., Ma, X., Wang, M., Zhang, Y., Gao, G., ... & Hou, S. (2018). Colorimetric and fluorescent probe for real-time detection of palladium (II) ion in aqueous medium and live cell imaging. Dyes and Pigments, 148, 286-291.
20. Wang, L., Zheng, X. Y., Zhang, X., & Zhu, Z. J. (2021). A quinoline-based fluorescent chemosensor for palladium ion (Pd^{2+})-selective detection in aqueous solution. Spectrochimica Acta Part A: Molecular and Biomolecular Spectroscopy, 249, 119283.
21. Lei, W. A. N. G., Wan-Yu, Z. H. U., & ZHANG, X. (2022). Selective and sensitive fluorescence detection of Pd (II) in 100% water and imaging application in living cells. Chinese Journal of Analytical Chemistry, 50(12), 100155.
22. Baig, M. Z. K., Pawar, S., Tulichala, R. P., Nag, A., & Chakravarty, M. (2017). A single fluorescent probe as systematic sensor for multiple metal ions: Focus on detection and bio-imaging of Pd^{2+}. Sensors and Actuators B: Chemical, 243, 226-233.
23. Ma, Z., Li, J., Lin, K., Ramachandran, M., Li, M., & Li, Y. (2020). Heterocyclic N-Oxides as Small-Molecule Fluorogenic Scaffolds: Rational Design and Applications of Their "On–Off" Fluorescence. Analytical chemistry, 92(18), 12282-12289.
24. Hirayama, T., Okuda, K., & Nagasawa, H. (2013). A highly selective turn-on fluorescent probe for iron (II) to visualize labile iron in living cells. Chemical science, 4(3), 1250-1256.
25. Niwa, M., Hirayama, T., Okuda, K., & Nagasawa, H. (2014). A new class of high-contrast Fe (II) selective fluorescent probes based on spirocyclized scaffolds for visualization of intracellular labile iron delivered by transferrin. Organic & biomolecular chemistry, 12(34), 6590-6597.
26. Reddy, C. R., Aila, M., Sathish, P., Mrinalini, M., Giribabu, L., Prasanthkumar, S., & Grée, R. (2019). Metal-free propargylation/aza-annulation approach to substituted β-carbolines and evaluation of their photophysical properties. Organic & Biomolecular Chemistry, 17(42), 9291-9304.
27. Hirayama, T., Tsuboi, H., Niwa, M., Miki, A., Kadota, S., Ikeshita, Y., ... & Nagasawa, H. (2017). A universal fluorogenic switch for Fe (ii) ion based on N-oxide chemistry permits the visualization of intracellular redox equilibrium shift towards labile iron in hypoxic tumor cells. Chemical science, 8(7), 4858-4866.
28. Sedenkova, K. N., Kolodyazhnaya, J. V., Vasilenko, D. A., Gracheva, Y. A., Kharitonoshvili, E. V., Grishin, Y. K., ... & Averina, E. B. (2019). Novel π-conjugated systems based on pyrimidine N-Oxide. Dyes and Pigments, 164, 72-81.
29. Knox, H. J., Hedhli, J., Kim, T. W., Khalili, K., Dobrucki, L. W., & Chan, J. (2017). A bioreducible N-oxide-based probe for photoacoustic imaging of hypoxia. Nature communications, 8(1), 1-9.
Preparation of artificial urine sample: Chandran, N., Janardhanan, P., Bayal, M., Pilankatta, R., & Nair, S. S. (2022). Development of a paper printed colorimetric sensor based on Cu-Curcumin nanoparticles for evolving point-of-care clinical diagnosis of sodium. Scientific reports, 12(1), 1-15.

exp_1179_2NH-NH2

Table 1 Crystal data and structure refinement for exp_1179_2NH-NH2.[CCDC No. 2194801]

Identification code exp_1179_2NH-NH2
Empirical formula C9H6N4O2
Formula weight 202.18
Temperature/K 293(2)
Crystal system monoclinic
Space group P21/c
a/Å 4.89130(10)
b/Å 9.7299(2)
c/Å 17.6911(4)
α/° 90
β/° 95.712(2)
γ/° 90
Volume/Å3 837.77(3)
Z 4
ρcalcg/cm3 1.603
μ/mm 1 1.009
F(000) 416.0
Crystal size/mm3 0.2 × 0.1 × 0.1
Radiation CuKα (λ = 1.54184)
2Θ range for data collection/° 10.05 to 159.082
Index ranges -3 ≤ h ≤ 6, -12 ≤ k ≤ 12, -22 ≤ l ≤ 20
Reflections collected 4265
Independent reflections 1751 [Rint = 0.0227, Rsigma = 0.0339]
Data/restraints/parameters 1751/0/141
Goodness-of-fit on F2 1.100
Final R indexes [I>=2σ (I)] R1 = 0.0416, wR2 = 0.1115
Final R indexes [all data] R1 = 0.0445, wR2 = 0.1148
Largest diff. peak/hole / e Å-3 0.21/-0.34

Table 2 Fractional Atomic Coordinates (×104) and Equivalent Isotropic Displacement Parameters (Å2×103) for exp_1179_2NH-NH2. Ueq is defined as 1/3 of of the trace of the orthogonalised UIJ tensor.

Atom	x	y	z	U(eq)
O1O	1630(2)	2293.6(10)	7220.4(6)	30.8(3)
O2O	7234(2)	5927.5(11)	5682.9(6)	30.0(3)
N1N	5868(2)	5049.1(11)	6030.3(6)	22.1(3)
N2N	2956(3)	8035.9(12)	6639.5(7)	31.4(3)
N3N	651(2)	4857.2(12)	7375.7(7)	25.0(3)
N4N	2982(2)	3154.4(11)	6827.6(6)	22.0(3)
C1C	5169(3)	1279.9(14)	6233.8(8)	26.7(3)
C2C	7002(3)	841.5(15)	5747.2(8)	31.8(3)

C3C	8483(3)	1785.5(16)	5347.7(8)	32.5(3)
C4C	8148(3)	3174.0(15)	5437.5(8)	27.5(3)
C5C	3988(3)	5462.8(13)	6496.1(7)	21.4(3)
C6C	3526(3)	6906.7(14)	6561.8(7)	23.6(3)
C7C	2513(3)	4513.3(13)	6910.9(7)	20.8(3)
C8C	4803(2)	2696.8(13)	6336.5(7)	21.7(3)
C9C	6286(3)	3641.6(13)	5935.1(7)	22.3(3)

Table 3 Anisotropic Displacement Parameters (Å2×103) for exp_1179_2NH-NH2. The Anisotropic displacement factor exponent takes the form: -2π2[h2a*2U11+2hka*b*U12+…].

Atom	**U11**	**U22**	**U33**	**U23**	**U13**	**U12**
O1O	35.1(5)	21.3(5)	38.6(6)	1.5(4)	16.3(4)	-8.1(4)
O2O	29.7(5)	28.8(5)	33.4(5)	8.4(4)	13.2(4)	-2.3(4)
N1N	21.0(5)	23.5(6)	22.4(5)	2.5(4)	5.2(4)	-0.8(4)
N2N	37.6(7)	22.6(6)	35.6(6)	0.5(5)	11.6(5)	-0.4(5)
N3N	28.0(6)	19.7(5)	29.2(6)	-1.6(4)	12.1(4)	-2.2(4)
N4N	22.3(5)	19.6(5)	24.8(5)	0.0(4)	6.0(4)	-2.7(4)
C1C	27.4(6)	22.5(6)	29.7(7)	-2.7(5)	1.4(5)	1.1(5)
C2C	34.2(7)	27.2(7)	33.5(7)	-6.9(6)	0.5(6)	7.7(6)
C3C	31.0(7)	39.0(8)	27.9(7)	-6.3(6)	5.3(5)	11.8(6)
C4C	25.1(6)	34.4(7)	23.5(6)	1.2(5)	5.8(5)	4.1(5)
C5C	21.4(6)	20.4(6)	23.0(6)	-0.7(5)	4.7(5)	-0.2(5)
C6C	24.2(6)	22.8(7)	24.8(6)	1.1(5)	6.8(5)	-2.0(5)
C7C	20.9(6)	19.9(6)	22.0(6)	-1.7(4)	3.6(5)	-0.7(5)
C8C	20.5(6)	22.6(6)	22.0(6)	-2.0(5)	1.9(5)	0.9(5)
C9C	21.6(6)	23.9(6)	21.5(6)	-0.5(5)	2.3(5)	2.3(5)

Table 4 Bond Lengths for exp_1179_2NH-NH2.

Atom	Atom	Length/Å	Atom	Atom	Length/Å
O1O	N4N	1.3088(14)	C1C	C2C	1.371(2)
O2O	N1N	1.2793(14)	C1C	C8C	1.4044(18)
N1N	C5C	1.3558(16)	C2C	C3C	1.403(2)
N1N	C9C	1.3973(17)	C3C	C4C	1.372(2)
N2N	C6C	1.1451(18)	C4C	C9C	1.4041(18)
N3N	C7C	1.3294(16)	C5C	C6C	1.4295(18)
N4N	C7C	1.3525(16)	C5C	C7C	1.4203(18)
N4N	C8C	1.3784(17)	C8C	C9C	1.4064(18)

Table 5 Bond Angles for exp_1179_2NH-NH2.

Atom	Atom	Atom	Angle/°	Atom	Atom	Atom	Angle/°
O2O	N1N	C5C	120.80(11)	C7C	C5C	C6C	120.32(12)
O2O	N1N	C9C	120.48(11)	N2N	C6C	C5C	174.27(14)
C5C	N1N	C9C	118.71(11)	N3N	C7C	N4N	116.58(12)
O1O	N4N	C7C	117.88(11)	N3N	C7C	C5C	124.77(12)
O1O	N4N	C8C	121.34(11)	N4N	C7C	C5C	118.64(11)
C7C	N4N	C8C	120.77(11)	N4N	C8C	C1C	119.83(12)

C2C	C1C	C8C	119.11(13)	N4N	C8C	C9C	120.34(12)
C1C	C2C	C3C	121.00(13)	C1C	C8C	C9C	119.83(12)
C4C	C3C	C2C	120.83(13)	N1N	C9C	C4C	120.32(12)
C3C	C4C	C9C	118.95(13)	N1N	C9C	C8C	119.40(11)
N1N	C5C	C6C	117.61(12)	C4C	C9C	C8C	120.28(13)
N1N	C5C	C7C	122.07(12)				

Table 6 Torsion Angles for exp_1179_2NH-NH2.

A	B	C	D	Angle/°	A	B	C	D	Angle/°
O1O	N4N	C7C	N3N	-1.60(17)	C2C	C1C	C8C	C9C	0.73(19)
O1O	N4N	C7C	C5C	179.23(11)	C2C	C3C	C4C	C9C	-0.2(2)
O1O	N4N	C8C	C1C	1.95(18)	C3C	C4C	C9C	N1N	-179.04(12)
O1O	N4N	C8C	C9C	-178.33(11)	C3C	C4C	C9C	C8C	0.3(2)
O2O	N1N	C5C	C6C	2.16(17)	C5C	N1N	C9C	C4C	177.84(11)
O2O	N1N	C5C	C7C	-177.63(11)	C5C	N1N	C9C	C8C	-1.51(18)
O2O	N1N	C9C	C4C	-2.06(18)	C6C	C5C	C7C	N3N	0.1(2)
O2O	N1N	C9C	C8C	178.59(10)	C6C	C5C	C7C	N4N	179.25(10)
N1N	C5C	C7C	N3N	179.94(12)	C7C	N4N	C8C	C1C	-177.23(11)
N1N	C5C	C7C	N4N	-0.96(19)	C7C	N4N	C8C	C9C	2.48(18)
N4N	C8C	C9C	N1N	-0.92(18)	C8C	N4N	C7C	N3N	177.62(11)
N4N	C8C	C9C	C4C	179.73(11)	C8C	N4N	C7C	C5C	-1.56(18)
C1C	C2C	C3C	C4C	0.4(2)	C8C	C1C	C2C	C3C	-0.7(2)
C1C	C8C	C9C	N1N	178.80(10)	C9C	N1N	C5C	C6C	-177.74(11)
C1C	C8C	C9C	C4C	-0.56(19)	C9C	N1N	C5C	C7C	2.47(18)
C2C	C1C	C8C	N4N	-179.55(12)					

Table 7 Hydrogen Atom Coordinates (Å×104) and Isotropic Displacement Parameters (Å2×103) for exp_1179_2NH-NH2.

Atom	x	y	z	U(eq)
H3NA	551.45	5696.89	7401.56	38
H3NB	-30(40)	4143(19)	7592(10)	30(4)
H1C	4182.55	647.43	6492.31	32
H2C	7268.17	-95.49	5680.85	38
H3C	9707.41	1465.87	5018.02	39
H4C	9139.1	3795.63	5172.94	33

Experimental

Single crystals of C9H6N4O2 [exp_1179_2NH-NH2] were []. A suitable crystal was selected and [] on a XtaLAB Pro: Kappa dual offset/far diffractometer. The crystal was kept at 293(2) K during data collection. Using Olex2 [1], the structure was solved with the olex2.solve [2] structure solution program using Charge Flipping and refined with the ShelXL [3] refinement package using Least Squares minimisation.

1. Dolomanov, O.V., Bourhis, L.J., Gildea, R.J, Howard, J.A.K. & Puschmann, H. (2009), J.

Appl. Cryst. 42, 339-341.
2. Bourhis, L.J., Dolomanov, O.V., Gildea, R.J., Howard, J.A.K., Puschmann, H. (2015). Acta Cryst. A71, 59-75.
3. Sheldrick, G.M. (2015). Acta Cryst. C71, 3-8.
Crystal structure determination of [exp_1179_2NH-NH2]
Crystal Data for C9H6N4O2 (M =202.18 g/mol): monoclinic, space group P21/c (no. 14), a = 4.89130(10) Å, b = 9.7299(2) Å, c = 17.6911(4) Å, β = 95.712(2)°, V = 837.77(3) Å3, Z = 4, T = 293(2) K, μ(CuKα) = 1.009 mm-1, Dcalc = 1.603 g/cm3, 4265 reflections measured (10.05° ≤ 2Θ ≤ 159.082°), 1751 unique (Rint = 0.0227, Rsigma = 0.0339) which were used in all calculations. The final R1 was 0.0416 (I > 2σ(I)) and wR2 was 0.1148 (all data).
Refinement model description
Number of restraints - 0, number of constraints - unknown.
Details:
1. Fixed Uiso
At 1.2 times of:
All C(H) groups
At 1.5 times of:
All N(H) groups
2.a Aromatic/amide H refined with riding coordinates:
C1C(H1C), C2C(H2C), C3C(H3C), C4C(H4C)
2.b Idealised tetrahedral OH refined as rotating group:
N3N(H3NA)
This report has been created with Olex2, compiled on 2018.05.29 svn.r3508 for OlexSys. Please let us know if there are any errors or if you would like to have additional features.